J. Fluid Mech. (1988), *vol.* 195, *pp.* 23–55
Printed in Great Britain

Fully developed pulsatile flow in a curved pipe

By COSTAS C. HAMAKIOTES AND STANLEY A. BERGER
Department of Mechanical Engineering, University of California, Berkeley, CA 94720, USA

(Received 22 June 1987 and in revised form 11 February 1988)

The fully developed region of periodic flows through curved pipes of circular cross-section and arbitrary curvature has been simulated numerically. The volumetric flow rate, prescribed by a cosine function, remains positive throughout the entire cycle. Such flows are characterized by three parameters: the frequency parameter α, the amplitude ratio γ and the mean Dean number κ_m. We use the Projection Method to solve the finite-difference approximation of the Navier–Stokes equations in their primitive form. The effect of κ_m on the flow has been extensively studied for the range $0.7559 \leqslant \kappa_m \leqslant 756$ for $\alpha = 15$ and $\gamma = 1$, and the curvature ratio, δ, equal to $\frac{1}{7}$. Interactions between the Stokes layer and the interior are noted and a variety of pulsatile motions along with reversal of the axial-flow direction are revealed. The manner in which the secondary motions evolve with increasing Dean number, and how they change direction from outward to inward 'centrifuging' at the centre, is also explained. Reversal in the axial flow is observed for all values of Dean number studied and occupies a region ranging from the area immediately adjacent to the entire wall for low values of Dean number to the entire inner half of the cross-section for larger values. When reversal of the axial flow is present, the local maximum axial shear stress is found at the inner bend where the backflow region is located. The values of circumferential shear stress for $\kappa_m = 0.7559$ and 151.2 confirm the existence of a single-vortex structure in the half-cross-section, whereas the values for larger values of mean Dean number are indicative of more complicated vortical structures.

1. Introduction

Unsteady flows in curved conduits are considerably more complex than those in straight conduits, and exhibit phenomena not yet fully understood. This work was greatly motivated by the practical importance of such flows along with questions raised regarding them. For example, as curved sections are present almost invariably in all piping systems it is important to know the pressure drop in the developing and fully developed parts of the flow if one is to predict the pumping power required to overcome curvature-induced pressure losses. Because the secondary motions in such flows enhance mixing within the fluid as well as heat transfer between the fluid and its surroundings, the magnitude of these effects is important in designing helically coiled chemical reactors or heat exchangers. For blood flow in the aortic arch, knowledge of shear-stress distributions and velocity profiles might improve the design of proper artificial heart valves or shed light on sites of cholesterol buildup on the vessel walls leading to atherosclerosis. There currently exist two schools of thought regarding these sites. Caro, Fitz-Gerald & Schroter (1971) claim that deposits occur in areas of low wall shear, while Fry (1968, 1973) suggests that they occur in areas of maximum wall shear. For a thorough review of recent developments

and the role of fluid mechanics in atherosclerosis the reader is referred to Nerem (1981) and Schettler *et al.* (1983).

For an extensive review of the entire subject of flow through curved pipes the reader may consult Berger, Talbot & Yao (1983), Itō (1987) and Nandakumar & Masliyah (1986). Periodic flows have been studied extensively during the past two decades. Until the present decade most studies have been either theoretical, involving some kind of perturbation, or experimental. Some of the most recent numerical studies are those by Lin & Tarbell (1980) and Rabadi, Simon & Chow (1980). Although in both cases the complete governing equations were solved, both works are limited to low secondary Reynolds-number values and small pressure-gradient variations, which render them inapplicable to aortic-arch flows. Chang & Tarbell (1985) obtained numerical results for flow conditions characteristic of the aortic arch. They solved, in their complete form, the axial momentum, the vorticity-transport and the stream-function equations to obtain results first-order accurate in time and second-order accurate in space.

In the current study we consider the unsteady laminar flow arising when a sinusoidal volumetric flow rate of the form

$$Q^*(t^*) = Q^*_{\mathrm{DC}} + Q^*_{\mathrm{AC}} \cos(\omega t^*) \tag{1.1}$$

is imposed through a pipe of circular cross-section, where ω denotes the frequency, and the asterisk indicates dimensional quantities. The fluid is assumed to be incompressible and Newtonian. We assume the tube profile is symmetric so that the flow in only half of the cross-section need be considered.

The work of Gong (1979) and Talbot & Gong (1983) has confirmed experimentally that a periodic flow entering a curved pipe does become fully developed, in the sense that it becomes periodic in time at any cross-section, and independent of axial position at some position downstream depending on curvature ratio, frequency parameter, and Reynolds number. Smith (1976) reported that in the case of steady flows through curved pipes the fully developed state is reached at distances along the curved tube much larger than the radius of the tube but much less than its radius of curvature. Our problem, therefore, is a two-dimensional one, treating only this fully developed region. Despite the two-dimensionality of the problem there are three velocity components to deal with, and all three momentum equations are required. Because of the fully developed assumption, however, the only axial-variation term which appears in the governing equations is the axial component of the pressure gradient needed to drive the flow. These unsteady Navier–Stokes equations are written in finite-difference form and solved numerically by the Projection Method (Chorin 1968).

The results we obtained are second-order accurate in time and space. We have chosen the frequency parameter and curvature ratio to model the flow of blood in the aorta. (The values of these parameters are also the ones intended by Gong 1979.) A positive volumetric flow rate with non-zero mean was imposed for the same reason. Motivated primarily by the transition of the secondary flow from outward to inward centrifuging, as reported by Lyne (1971) at the limit of certain parameters, and by the study of Smith (1975), we studied extensively the effect of the Reynolds number on the flow. The flow patterns for $Re_{\mathrm{m}} = 400$ (and $Re_{\mathrm{m}} = 500$, Hamakiotes 1987) are in very good qualitative and quantitative agreement with Gong's (1979) experiments, and the pressure gradient leads the volumetric flow rate by about 90°. Throughout our calculations we found that the phase difference between pressure gradient and

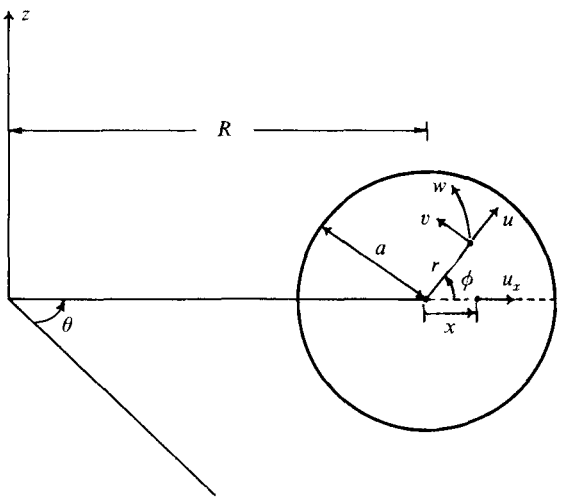

FIGURE 1. Toroidal coordinate system.

flow rate remained constant, independent of Reynolds number, which is consistent with Uchida's (1956) findings that the phase difference is a function of the frequency parameter alone. The results also exhibit qualitative agreement with Lyne's (1971) results and Smith's (1975) cases III and IX. Owing to the theoretical nature of the latter two studies their results are asymptotically valid in the limits of certain parameters. This is discussed further in §4.

2. Mathematical formulation

2.1. *Governing equations*

The equations of motion in conservative, dimensionless form, for momentum and mass, in a toroidal coordinate system (figure 1) are

$$St_{\mathrm{m}}\frac{\partial u}{\partial t}+\frac{1}{rB}\left[\frac{\partial}{\partial r}(rBu^2)+\frac{\partial}{\partial\phi}(Buv)-Bv^2-\delta rw^2\cos\phi\right]$$
$$=-\frac{\partial P}{\partial r}+\frac{1}{Re_{\mathrm{m}}}\left\{\frac{1}{rB}\left[\frac{\partial}{\partial r}\left(rB\frac{\partial u}{\partial r}\right)+\frac{\partial}{\partial\phi}\left(\frac{B}{r}\frac{\partial u}{\partial\phi}\right)\right]\right.$$
$$\left.-\frac{1}{r^2}\left(2\frac{\partial v}{\partial\phi}+u\right)+\frac{\delta v\sin\phi}{rB}+\frac{\delta^2\cos\phi}{B^2}(v\sin\phi-u\cos\phi)\right\}, \quad (2.1)$$

$$St_{\mathrm{m}}\frac{\partial v}{\partial t}+\frac{1}{rB}\left[\frac{\partial}{\partial r}(rBuv)+\frac{\partial}{\partial\phi}(Bv^2)+Buv+\delta rw^2\sin\phi\right]$$
$$=-\frac{1}{r}\frac{\partial P}{\partial\phi}+\frac{1}{Re_{\mathrm{m}}}\left\{\frac{1}{rB}\left[\frac{\partial}{\partial r}\left(rB\frac{\partial v}{\partial r}\right)+\frac{\partial}{\partial\phi}\left(\frac{B}{r}\frac{\partial v}{\partial\phi}\right)\right]\right.$$
$$\left.+\frac{1}{r^2}\left(2\frac{\partial u}{\partial\phi}-v\right)-\frac{\delta u\sin\phi}{rB}-\frac{\delta^2\sin\phi}{B^2}(v\sin\phi-u\cos\phi)\right\}, \quad (2.2)$$

$$St_{\mathrm{m}}\frac{\partial w}{\partial t}+\frac{1}{rB}\left[\frac{\partial}{\partial r}(rBuw)+\frac{\partial}{\partial\phi}(Bvw)+\delta rw(u\cos\phi-v\sin\phi)\right]$$
$$=-\frac{\delta}{B}\frac{\partial P}{\partial\theta}+\frac{1}{Re_{\mathrm{m}}}\left\{\frac{1}{rB}\left[\frac{\partial}{\partial r}\left(rB\frac{\partial w}{\partial r}\right)+\frac{\partial}{\partial\phi}\left(\frac{B}{r}\frac{\partial w}{\partial\phi}\right)\right]-\frac{w\delta^2}{B^2}\right\}, \quad (2.3)$$

$$\frac{\partial}{\partial r}(rBu)+\frac{\partial}{\partial\phi}(Bv)=0, \quad (2.4)$$

where $\delta = a/R$ and $B = 1+\delta r\cos\phi$. Re_{m} is the mean Reynolds number, defined as $Re_{\mathrm{m}} = aW_{\mathrm{DC}}/\nu$, and St_{m} is the mean Strouhal number, defined as $St_{\mathrm{m}} = a\omega/W_{\mathrm{DC}}$.

Dimensionless variables are defined by

$$\boldsymbol{V}=\frac{\boldsymbol{V}^*}{W_{\mathrm{DC}}},\quad P=\frac{P^*}{\rho W_{\mathrm{DC}}^2},\quad \boldsymbol{r}=\frac{\boldsymbol{r}^*}{a},\quad t=\omega t^*,\quad \boldsymbol{\tau}=\frac{\alpha\boldsymbol{\tau}^*}{\mu W_{\mathrm{DC}}}, \quad (2.5)$$

where the asterisk indicates dimensional quantities, $\boldsymbol{r}$ is the position vector, μ is the coefficient of viscosity, ν is the kinematic viscosity, ρ is the density, $\boldsymbol{V}$ is the velocity vector, P is the pressure, t is the time, $\boldsymbol{\tau}$ is the viscous-stress tensor and $W_{\mathrm{DC}} = Q_{\mathrm{DC}}/\pi a^2$. The reference velocity, W_{DC}, corresponds to the volumetric flow rate Q_{DC} pumped through a cross-sectional area πa^2, and can be alternatively referred to as the time-mean value of the axial velocity. Here, a is the radius of the pipe (figure 1), and a volumetric flow rate of the form $Q(t) = Q_{\mathrm{DC}}+Q_{\mathrm{AC}}\cos(t)$ is assumed.

From the above equations we deduce that the flow is governed by the following three parameters:

(i) The *frequency parameter*, $\alpha = a(\omega/\nu)^{\frac{1}{2}} = (Re_{\mathrm{m}}St_{\mathrm{m}})^{\frac{1}{2}}$. This parameter can be physically interpreted in two ways: as the ratio of the pipe radius a to the Stokes-layer thickness $(\nu/\omega)^{\frac{1}{2}}$, or as the square root of the ratio of a viscous diffusion time a^2/ν to the period of the oscillation $1/\omega$. A small value of α implies a large viscous layer near the wall compared with a small inviscid core near the centre, or, alternatively, a large oscillation period compared with the viscous diffusion time, and therefore quasi-steady flow. The inverse of these conclusions would be drawn in the case of a large value of α. A conclusion drawn by Zalosh & Nelson (1973) was that as the value of α increases, the secondary convective mixing of the fluid increases also. Fluid particles initially near the tube axis migrate to the tube wall. Because of smaller secondary velocities, this excursion becomes smaller for increasing α and the time required for a fluid particle to return to its original cross-sectional position increases. Thus α plays an important role in heat and mass transfer, although an optimum value is not obvious.

(ii) The *mean Dean number*, $\kappa_{\mathrm{m}} = 2Re_{\mathrm{m}}\delta^{\frac{1}{2}}$. Physically, the Dean number is the ratio of the square root of the product of the inertia and centrifugal forces to the viscous forces. Since the secondary flows in curved pipes arise primarily owing to centrifugal forces, which, in turn, originate from curvature effects, we expect the magnitude of the secondary motions to be linked to the curvature ratio δ. Because δ is a direct measure of the effect of the pipe geometry it affects the balance between the three forces, inertia, viscous and centrifugal. Although the effect of δ has not been studied extensively, it can have a major effect on the flow.

(iii) The *amplitude ratio*, γ. This is the ratio of the alternating to the steady component of the volumetric flow rate. A small value of γ would suggest quasi-steady

Name	Definition
Curvature ratio	$\delta = a/R$
Amplitude ratio	$\gamma = Q_{AC}/Q_{DC}$
Mean Strouhal number	$St_m = \dfrac{\omega a}{W_{DC}}$
Mean Reynolds number	$Re_m = \dfrac{W_{DC}\, a}{\nu}$
Mean Dean number	$\kappa_m = \dfrac{2W_{DC}\, a}{\nu}(a/R)^{\frac{1}{2}} = 2Re_m\, \delta^{\frac{1}{2}}$
Secondary Reynolds number	$R_s = \dfrac{W_{DC}^2\, a}{R\omega\nu} = \dfrac{Re_m}{St_m}\delta$
Frequency parameter	$\alpha = a(\omega/\nu)^{\frac{1}{2}} = (St_m\, Re_m)^{\frac{1}{2}}$

TABLE 1. Flow parameters

flow. We can see the origins of this parameter if we recall the non-dimensionalization of the velocity field:

$$V = \frac{V^*}{W_{DC}} = O\left(\frac{\int V^* \cdot \boldsymbol{n}\, da}{\int W_{DC}\, da}\right) = \frac{Q}{Q_{DC}} = \frac{Q_{DC} + Q_{AC}\cos(t)}{Q_{DC}} = 1 + \gamma\cos(t),$$

where the integrals are over the cross-sectional area of the pipe.

These, and other pertinent parameters of the problem, are listed in table 1.

2.2. *Boundary conditions*

Initial condition. Singh (1974) used as the initial condition for his analysis of the steady entry flow into a curved pipe an inviscid vortex with its origin at the centre of curvature. Later, the experiments of Agrawal (1975), Agrawal, Talbot & Gong (1978) and Choi, Talbot & Cornet (1979) showed that such a profile almost immediately developed at the entrance even if the flow entered with uniform velocity. We use, therefore, such an inviscid-like vortex profile to initialize the velocity field:

$$w(r, \phi, t = 0) = \frac{1}{1 + \delta r\cos\phi}, \quad u(r, \phi, t = 0) = v(r, \phi, t = 0) = 0. \tag{2.6}$$

The corresponding pressure field, obtained from the Bernoulli equation, is

$$P = -\frac{1}{2}\frac{1}{(1 + \delta r\cos\phi)^2}. \tag{2.7}$$

Rigid wall. All three components of the velocity field are set to zero on the wall owing to the no-slip condition

$$u(1, \phi, t) = v(1, \phi, t) = w(1, \phi, t) = 0. \tag{2.8}$$

Plane of symmetry. For the range of Reynolds numbers, or equivalently Dean numbers, that we are examining, the flow exhibits symmetry across the centreplane, as has been confirmed by Gong's (1979) experiments. (New findings cast doubt on the symmetry at higher Reynolds numbers (Winters 1984; Winters & Brindley 1984).)

Consequently, we need solve the Navier–Stokes equations for the half domain $0 \leqslant \phi \leqslant \pi$ only. The symmetry conditions are

$$\frac{\partial u}{\partial \phi} = \frac{\partial w}{\partial \phi} = 0, \quad v = 0 \quad \text{at } \phi = 0, \pi. \tag{2.9}$$

Fully developed flow. All streamwise derivatives are set to zero, except for that of the pressure, i.e.

$$\frac{\partial u}{\partial \theta} = \frac{\partial v}{\partial \theta} = \frac{\partial w}{\partial \theta} = 0. \tag{2.10}$$

Incompressibility. This condition is necessary because the problem is two-dimensional but there are three velocity components. We integrate the velocity over the cross-section noting that it must integrate to the specified volumetric flow rate. In this manner, the pressure gradient necessary to sustain the flow is calculated. In this case, the condition is

$$Q^*(t^*) = Q^*_{\mathrm{DC}} + Q^*_{\mathrm{AC}} \cos(\omega t^*) = 2 \int_0^{\pi} \int_0^{a} w^* r^* \, \mathrm{d}r^* \, \mathrm{d}\phi.$$

Once again, the asterisk denotes dimensional quantities. Non-dimensionalizing using (2.5), and for Q, Q_{DC} and Q_{AC} using $Q_{\mathrm{DC}} = \pi a^2 W_{\mathrm{DC}}$, we obtain

$$Q(t) = 1 + \gamma \cos(t) = \frac{2}{\pi} \int_0^{\pi} \int_0^{1} wr \, \mathrm{d}r \, \mathrm{d}\phi. \tag{2.11}$$

3. Numerical formulation

3.1. *The projection method*

To solve equations (2.1)–(2.4) we use Chorin's (1968) Projection Method. The method consists of the steps outlined below:

$$\frac{\boldsymbol{V}^* - \boldsymbol{V}^n}{\Delta t} + \frac{1}{St_{\mathrm{m}}}((\boldsymbol{V}\cdot\boldsymbol{\nabla})\,\boldsymbol{V} + \boldsymbol{V}(\boldsymbol{\nabla}\cdot\boldsymbol{V})) - \frac{1}{St_{\mathrm{m}}\,Re_{\mathrm{m}}}\nabla^2 \boldsymbol{V}^n = 0, \tag{3.1}$$

$$\frac{1}{St_{\mathrm{m}}}\nabla^2 P^{n+1} = \frac{1}{\Delta t}\boldsymbol{\nabla}\cdot\boldsymbol{V}^*, \tag{3.2a}$$

$$\left(\frac{\partial P}{\partial N}\right)^{n+1}_{\Gamma} = -\frac{St_{\mathrm{m}}}{\Delta t}(\boldsymbol{V}^{n+1} - \boldsymbol{V}^*)_{\Gamma}\cdot\boldsymbol{N}, \tag{3.2b}$$

$$\frac{\boldsymbol{V}^{n+1} - \boldsymbol{V}^*}{\Delta t} + \frac{1}{St_{\mathrm{m}}}\boldsymbol{\nabla} P^{n+1} = 0. \tag{3.3a}$$

Here the asterisk indicates a provisional, or auxiliary, time step t^* and corresponding values of each quantity. The superscripts, n and $n+1$, indicate the time steps at which the superscripted quantities are to be evaluated. $\boldsymbol{N}$ is the outward unit vector normal to the boundary Γ of the flow domain.

We see that at the first step the momentum equation is solved without the pressure gradient to obtain an auxiliary velocity field $\boldsymbol{V}^*$. This velocity field is not physically a meaningful field as it does not come from the correct momentum equations. In the second step the Poisson-type equation (3.2a) is solved for the correct pressure at the next time step, P^{n+1}. The proper boundary condition to be used with this equation

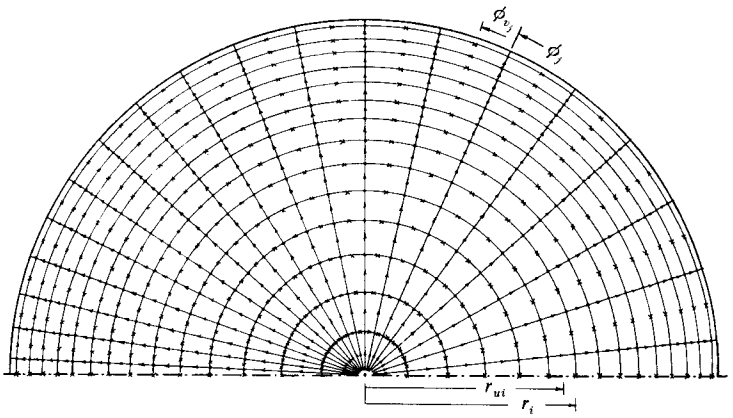

FIGURE 2. Grid system in cross-section: ●, pressure and axial velocity; ×, circumferential velocity; ↑, radial velocity.

in the continuous case is given by (3.2*b*) and is derived by projecting the vector equation (3.3*a*) on $\boldsymbol{N}$. In the discrete case, (3.2*a*) is to be solved subject to (3.3*a*) and $\boldsymbol{\nabla} \cdot \boldsymbol{V}^{n+1} = 0$. Finally, in the last step, the correct velocity field at the next time step $\boldsymbol{V}^{n+1}$ is obtained by solving (3.3*a*).

Thus in the Projection Method one first obtains a global velocity field $\boldsymbol{V}^*$, which is not divergence-free, which is then projected, hence the name of the method, on a divergence-free domain to yield a physical, divergence-free, velocity field $\boldsymbol{V}^{n+1}$. The divergence-free character of this velocity field can be seen if we take the divergence of (3.3*a*), making use of (3.2*a*).

3.2. *Implementation of the projection method*

To write the continuity and momentum equations (2.1)–(2.4) in a computational finite-difference scheme we discretize the domain of interest, the half-cross-section, using a non-uniform staggered mesh. The mesh is constructed in such a way that the pressure is defined at the centre of the cell while the three velocity components, u, v and w, are defined at different positions on the boundaries of the pressure cell, as indicated on figures 2 and 3. Because previous work on this problem suggests that the flow structure is complicated in the region of the inner bend, $\phi = 180°$, the mesh is made finer near the inner bend and coarser as we proceed towards the outer bend. For the radial direction, because of the boundary layer growing on the wall, $r = 1$, a finer grid is required in this region than in the core where no drastic velocity changes occur.

Time increments were chosen to be uniform for all the simulations presented. Chang & Tarbell (1985) used 82 time steps per period for sinusoidal-flow simulations and 164 steps per period for pulsatile-flow simulations. In our simulations 400 time steps per period are used.

To evaluate the auxiliary velocity field, $\boldsymbol{V}^*$, we have sought implicit schemes which are convenient to use, and accurate to $O(\Delta t^2) + O(\Delta x^2)$, where Δx is any one of the three space increments Δx_i, $i = 1, 2, 3$. We decided on the Douglas & Gunn (1964) ADI method (see also Douglas 1962). Throughout the calculations centred differencing in space is used. The method is unconditionally stable. An important advantage of ADI methods is that both steps lead to tridiagonal matrices, for which

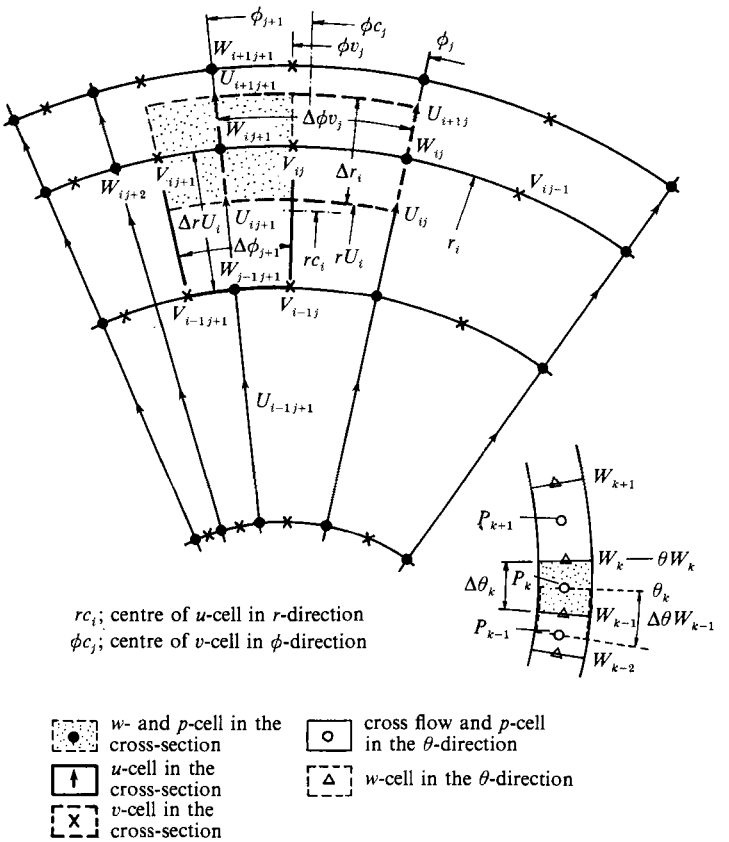

FIGURE 3. Velocity and pressure cells.

fast and efficient methods of solution have been developed. In the Thomas algorithm used here the tridiagonal matrix is converted into an upper triangular matrix which is solved by direct backward substitution.

The boundary conditions for V^* are derived from (3.3a), rewritten as

$$V^* = V^{n+1} + \frac{\Delta t}{St_m} \mathbf{G} P^{n+1}, \tag{3.3b}$$

where $\mathbf{G}$ denotes an approximation to the gradient operator. Because the pressure at the next time step, $n+1$, is not yet known, we use a Taylor-series expansion:

$$\mathbf{G}P^{n+1} = \mathbf{G}P^n + \Delta t \frac{\partial \mathbf{G}P}{\partial t} + O(\Delta t^2). \tag{3.4}$$

We then substitute (3.4) for the pressure gradient at the time step t^{n+1} into (3.3b) to get an expression to evaluate the boundary conditions for the auxiliary velocity field in terms of known quantities:

$$V^* = V^{n+1} + \frac{\Delta t}{St_m} \mathbf{G}P^n + O(\Delta t^2). \tag{3.5}$$

The pressure is evaluated from the Poisson-type equation (3.2a) subject to the boundary condition (3.2b). We use the method of successive over-relaxation. Note

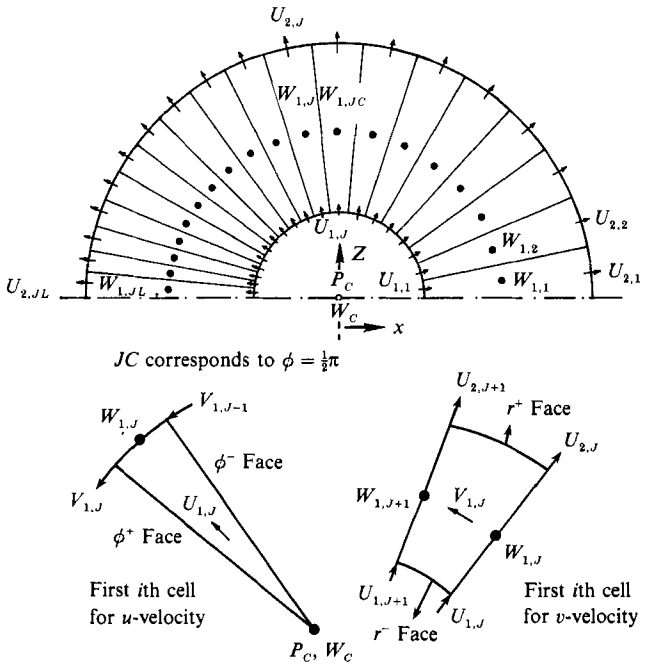

FIGURE 4. Centre cell for the pressure and the axial velocity.

that this Poisson equation for the pressure results from taking the divergence of (3.3*b*) and using the equation of continuity, $\nabla \cdot V = 0$.

The last step of the calculations is the evaluation of the velocity field, V^{n+1}, at the next time step, t^{n+1}. The two secondary components of the velocity u, and v, are calculated explicitly from the corresponding components of (3.3*b*) by direct substitution for the known quantities

$$u^{n+1} = u^* - \frac{\Delta t}{St_m} \frac{\partial P^{n+1}}{\partial r}, \quad v^{n+1} = v^* - \frac{\Delta t}{St_m} \frac{1}{r} \frac{\partial P^{n+1}}{\partial \phi}. \tag{3.6}$$

The calculation of the axial velocity component, w, is more subtle. Unlike the two secondary velocities, the axial component cannot be calculated from the axial component of (3.3*b*) since the assumption of fully developed flow prevents us from evaluating the pressure as a function of the axial direction, and the physics of the problem suggests that the axial pressure gradient, $\partial P/\partial \theta$, is a function of time only. Taking these facts into account we proceed as follows: first we integrate the axial component of the vector equation (3.3*b*):

$$\int_0^\pi \int_0^1 (w^{n+1} - w^*)\, r \, dr \, d\phi = -\frac{\delta \Delta t}{St_m} \frac{\partial P^{n+1}}{\partial \theta} \int_0^\pi \int_0^1 \frac{1}{B} r \, dr \, d\phi. \tag{3.7}$$

We now note that w^{n+1} must integrate over the cross-sectional area, at any time, to the specified volumetric flow rate. At this point the incompressibility condition, (2.11), is used to give an analytic value for this integral. The integral of the auxiliary axial velocity component, w^*, is performed numerically. Finally, since the axial pressure gradient is uniform over the cross-section, it can be removed from the

integral and, being the only unknown in the equation, can be solved for directly. Then w^{n+1} is calculated from the axial component of (3.3*b*),

$$w^{n+1} = w^* - \frac{\Delta t}{St_m} \frac{\delta}{B} \frac{\partial P^{n+1}}{\partial \theta}. \tag{3.8}$$

The centre of the pipe, $r = 0$, is a mathematical singularity, not a physical one, as both the velocity and pressure fields are well behaved there. The staggered nature of our mesh, however, requires that a nodal point be placed at the centre. For this cell with centre at $r = 0$ special care has to be taken to assure conservation of mass and axial momentum. We do not have to concern ourselves with the other two momentum components as their corresponding cells are not located on the centre (figure 4). For our treatment of the centre we use an integral analysis patterned after that of Soh (1983), where the reader can find more detail about the procedure.

Soh's calculations were all explicit; the ones reported here are implicit. This can pose a problem when we treat the centre, and try to incorporate it in the remainder of the calculations. For example, the very important advantage of ADI methods, that they yield tridiagonal matrices, whose properties and solution methods are well known, would be in jeopardy if we treated the centre implicitly. To avoid this we treat the centre explicitly, using an Allen & Cheng-type (1970) time-splitting technique, following Soh (1983).

For the details of the numerical calculations, the interested reader may consult Hamakiotes (1987).

4. Results and discussion

4.1. *Preliminaries*

The flow-field development has been calculated for the range of Reynolds numbers listed in table 2; a portion of these results is included and discussed here. The curvature ratio, amplitude ratio and frequency parameter were chosen to have the values $\frac{1}{7}$, 1 and 15, respectively. Calculations were first carried out for $Re_m = 1$, the initial velocity field being that of an inviscid vortex with its origin at the centre of curvature. Upon convergence these results were used to initialize the velocity field for the next higher Reynolds number. This continued up to $Re_m = 1000$. The algorithm was tested and proved to converge to the same velocity field regardless of the manner in which the velocity field was initialized. When this initial field had uniform axial velocity, and zero secondary velocity the algorithm proceeded to the final, correct results after evolving through an inviscid vortex profile. When this potential vortex profile was used to initialize the field, the algorithm converged fastest.

The successive over-relaxation iterations for the pressure were stopped when the relative change in pressure converged to within less than 10^{-7}. In fact, it was first verified that the pressure could be made to converge to machine accuracy, but we chose not to impose this extreme degree of accuracy to save computing time. Roughly 90 iterations per time step were required.

The scheme used is iterative in the sense that integration of the governing equations is carried out for a number of cycles until periodicity of results is achieved. Experimentation showed that whereas it only takes about 10 cycles for the relative change in the axial component of the velocity and the pressure to each converge to less than 10^{-4}, it takes three to four times as many cycles for the relative changes in

$\delta = \frac{1}{7}$, $\alpha = 15$, $\gamma = 1$

Re_m	St_m	R_s	κ_m
1	225.0	6.349×10^{-4}	0.7559
50	4.500	1.587	37.80
100	2.250	6.349	75.59
200	1.125	25.40	151.2
300	0.7500	57.14	226.8
400	0.5625	101.6	302.4
500	0.4500	158.7	378.0
1000	0.2250	635.0	756.0

TABLE 2. Parameter values of flow calculations

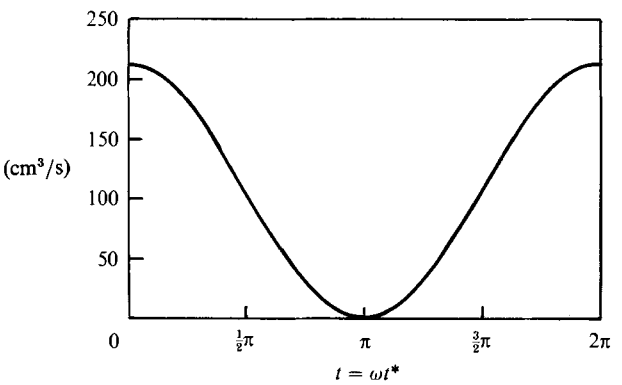

FIGURE 5. Volumetric flow rate.

the two secondary components of the velocity to converge to less than 10^{-3}. If the calculation is continued until the two secondary velocities converge to less than the set criterion of 10^{-3}, we find that the axial velocity and the pressure have converged to better than 10^{-7} or 10^{-8}.

The assumed volumetric flow rate is shown in figure 5. The resulting local – at each grid point – and global – the sum of all local values – divergence was calculated to be between 10^{-6} and 10^{-10} at all times. The fact that the divergence is of the same order of magnitude as the error in the pressure further validates the numerical procedure employed. The numerically computed flow rate was calculated to be within less than 2×10^{-4}% of the analytic flow rate at all times for all values of mean Reynolds numbers.

Each time cycle was subdivided into 400 time steps, so $\Delta t = 2\pi/400$. A non-uniform staggered 14×19 mesh, in the radial and circumferential direction respectively, was used to discretize the physical domain of the half-cross-section. Centred differencing in space was used, accounting for the stability and second-order accuracy of the code. The effect of grid refinement was also studied. Increasing the mesh points to 24×24 changes the results only very slightly. The 14×19 grid system is the same as that used by Soh (1983). The calculations were carried out on the IBM 3081 and 3090 at the University of California, Berkeley. It required about 3 min of CPU time to complete a cycle.

The results are shown on figures 6–10. Each consists of a series of six parts, (*a*)–(*f*). Part (*a*) of each figure shows the calculated pressure gradient (with its

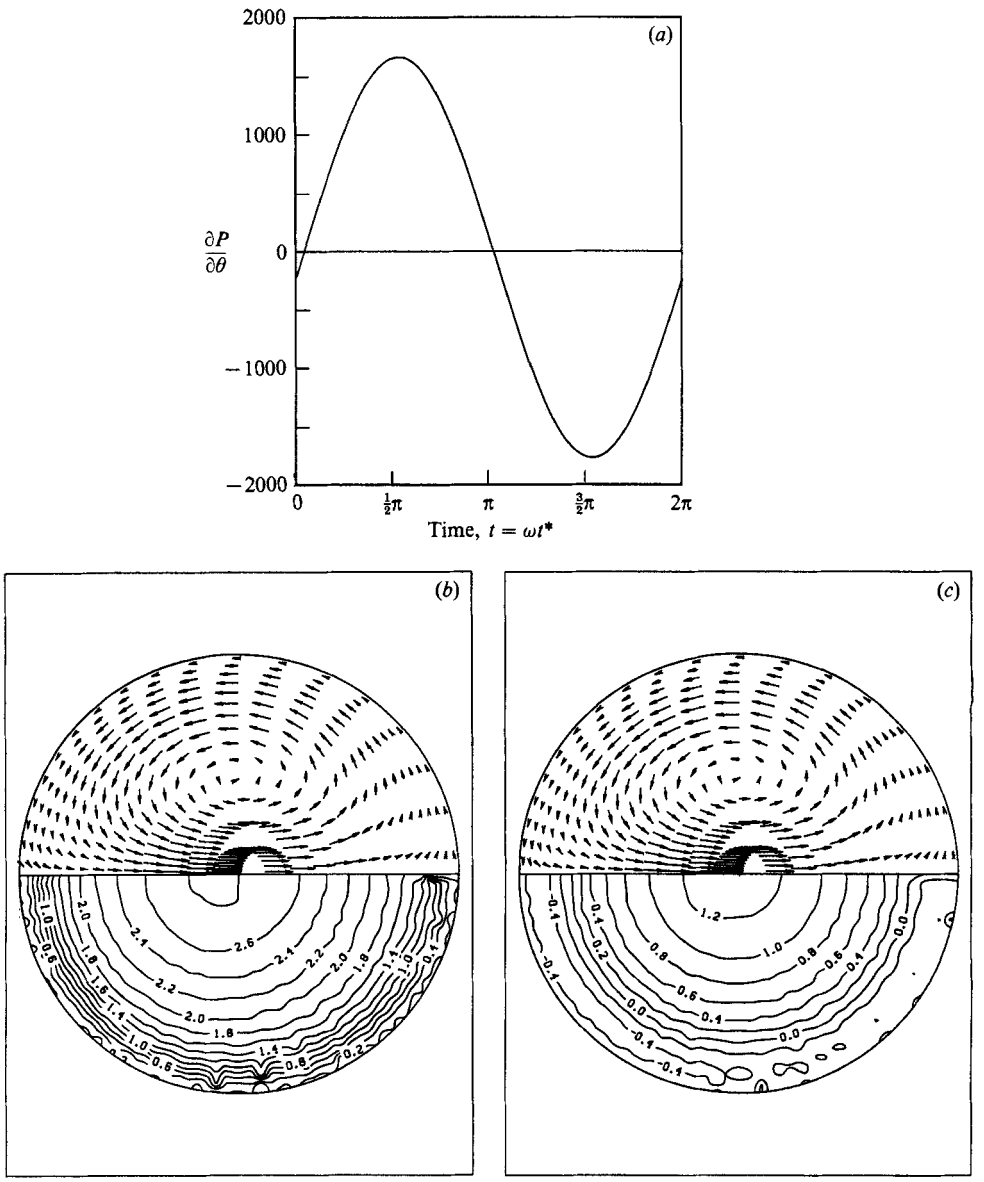

FIGURE 6(*a–c*). For caption see facing page.

algebraic sign) for the imposed volumetric flow rate. Hence, the pressure gradient driving the flow is the negative of what is shown. Consistent with previous work (Uchida 1956), we find that the pressure gradient driving the flow leads the volumetric flow rate by about 90° regardless of Reynolds number. The following five parts, (*b*)–(*f*), show the flow-field development over the cycle for the corresponding value of mean Reynolds number. The times at which the results are shown correspond to the cycle of figure 5. On each of the figures 6–10, (*b*)–(*f*), the left-hand side corresponds to the inner bend and the right-hand side to the outer bend. Because of the assumed symmetry of the flow with respect to the centreplane, on the upper half are plotted the secondary-velocity vectors, on the lower half the axial isovelocity

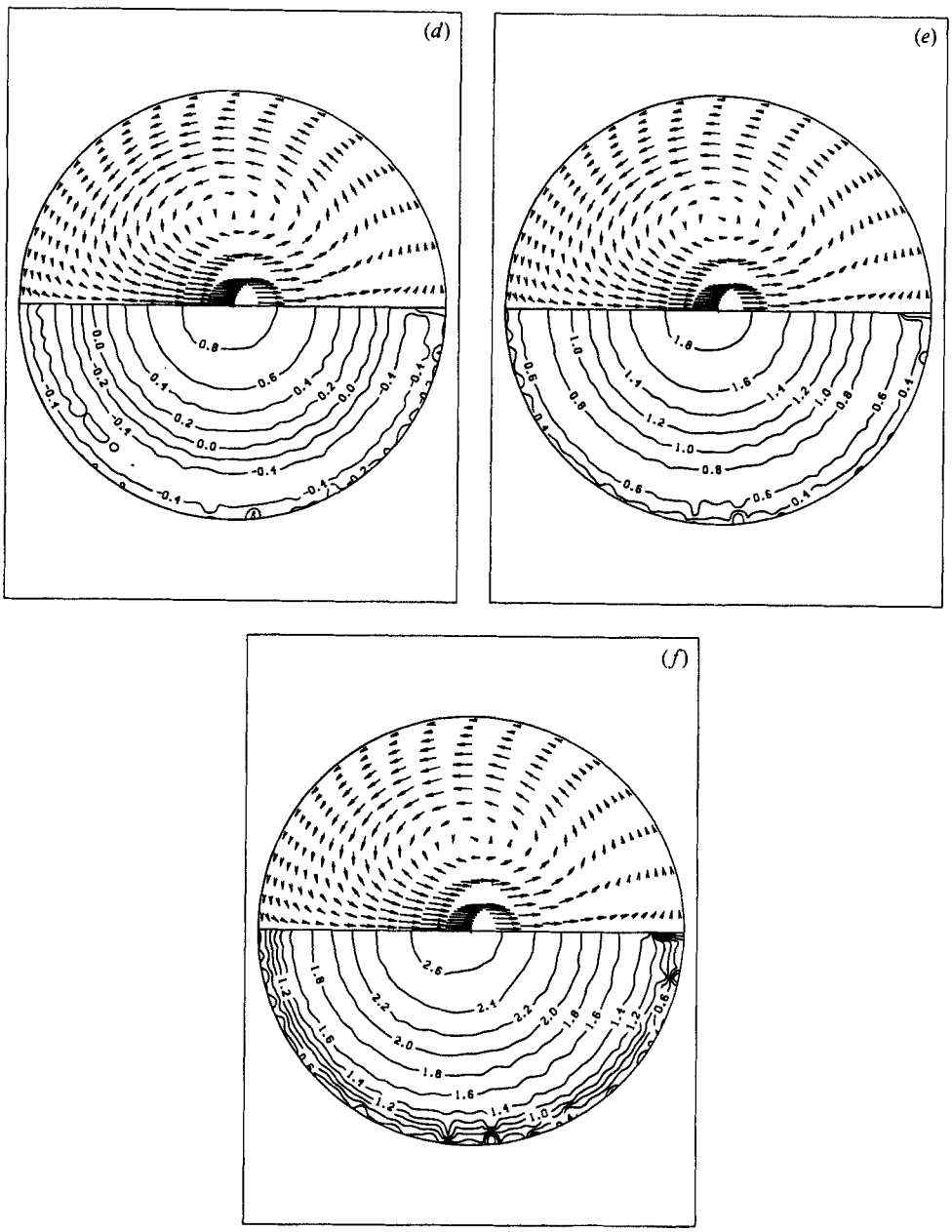

FIGURE 6. (*a*) Calculated axial pressure gradient for $Re_m = 1$. (*b–f*) Secondary-velocity vectors and axial isovelocity contours for $Re_m = 1$, $\lambda = 18$: (*b*) $\omega t^* = \frac{1}{4}\pi$; (*c*) $\frac{3}{4}\pi$; (*d*) π; (*e*) $\frac{3}{2}\pi$; (*f*) $\frac{7}{4}\pi$.

contours. To keep the secondary-velocity vectors reasonably sized and so that they do not extend beyond the cross-section, they are multiplied by a scaling factor, λ, whose value varies with Reynolds number and is listed in each of the figures. A vector of length equal to the radius of the pipe would correspond to a secondary velocity of magnitude $1/\lambda$. Note that all figures refer to dimensionless quantities.

Figures 11 and 12 are sets consisting of four parts each showing the axial and

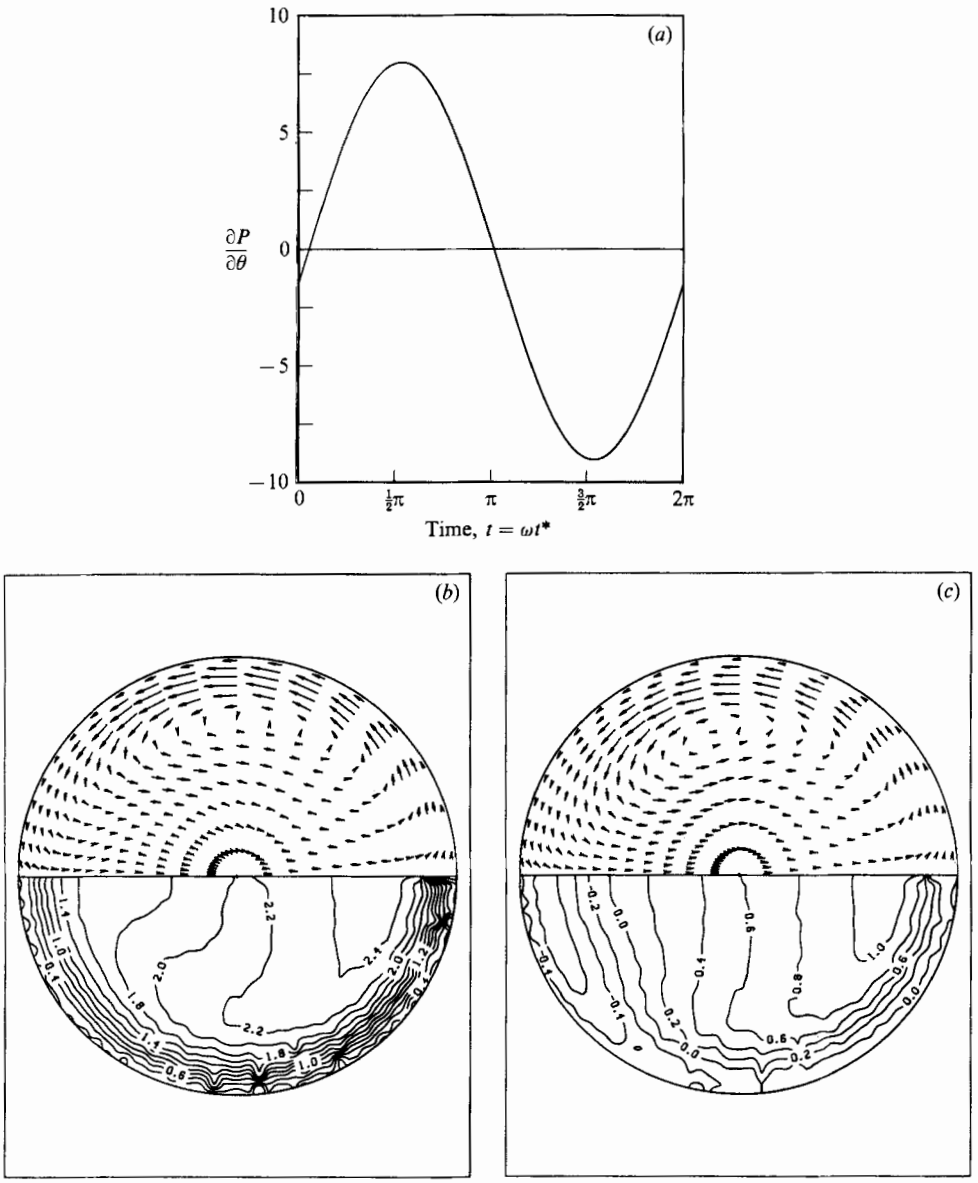

FIGURE 7 (*a–c*). For caption see facing page.

circumferential component of the shear stress, respectively. They are intended to illustrate the temporal development over the cycle of these shear-stress components for each value of Reynolds number considered.

For the sake of clarity, we note that from now on when we use the terms 'acceleration' and 'deceleration' we refer to the volumetric flow rate as shown in figure 5, not to the axial pressure gradient.

A complete set of all our results is presented in Hamakiotes (1987). For quantitative validation of our computational procedure we have compared our results with the experiments of Gong (1979). In his second experiment Gong used $\delta = \frac{1}{7}$, $\gamma = 1.02$, $\alpha = 12.5$, and $\kappa_m = 372$. The closest case to his that we simulated was for the values $\delta = \frac{1}{7}$, $\gamma = 1$, $\alpha = 15$, and $\kappa_m = 378$. We have verified that when Gong's

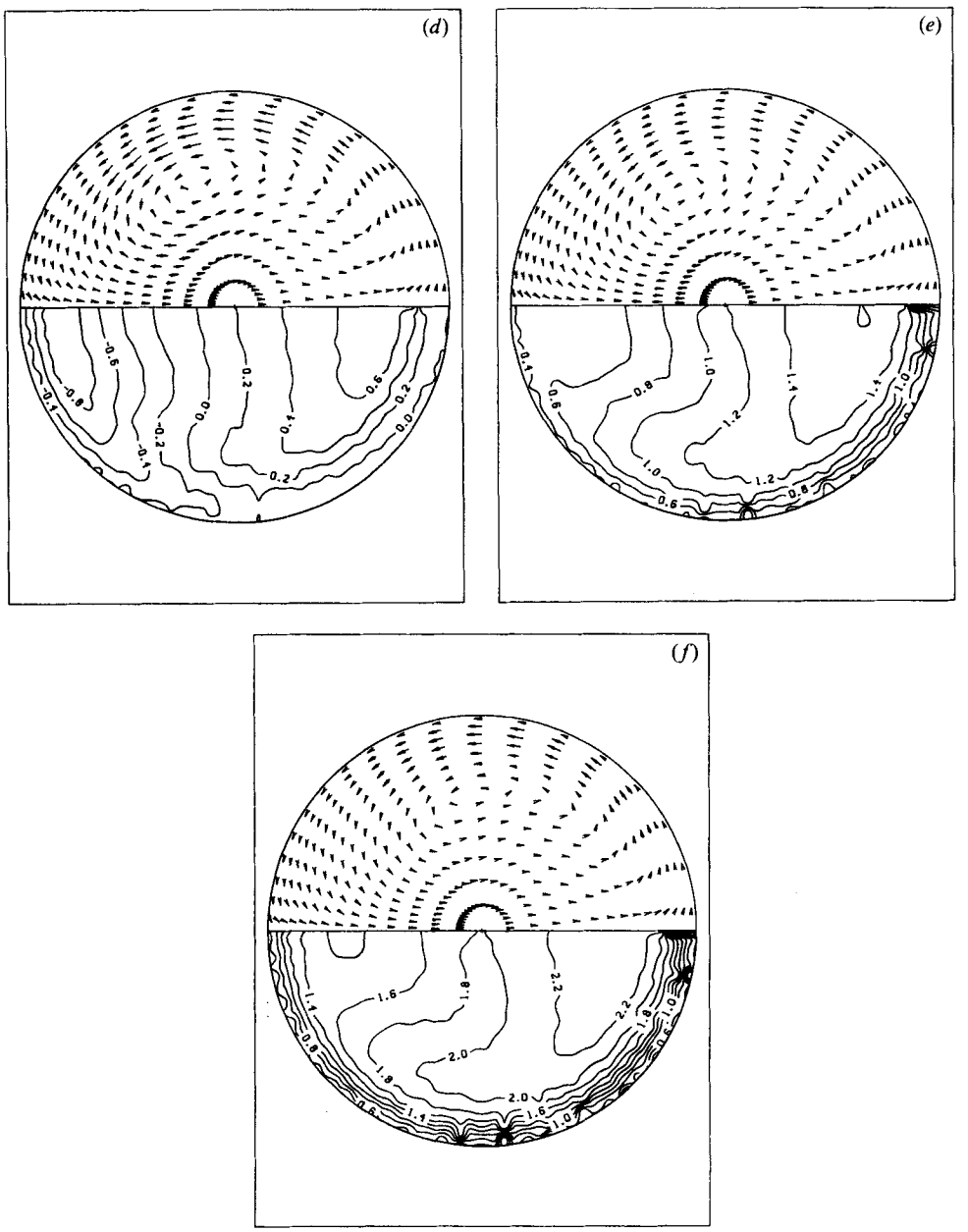

FIGURE 7. (*a*) Calculated axial pressure gradient for $Re_m = 200$. (*b–f*) Secondary-velocity vectors and axial isovelocity contours for $Re_m = 200$, $\lambda = 0.4$: (*b*) $\omega t^* = \frac{1}{4}\pi$; (*c*) $\frac{3}{4}\pi$; (*d*) π; (*e*) $\frac{3}{2}\pi$; (*f*) $\frac{7}{4}\pi$.

results are non-dimensionalized they are in very good agreement with ours considering the very minor difference in Dean number and the somewhat more substantial difference in the frequency parameter.

4.2. *Flow-field development*

We start with the flow-field development over the cycle for $Re_m = 1$. The results are shown in figure 6 (*a–f*). Figure 6 (*a*) depicts the computed pressure gradient necessary

to drive the flow corresponding to the imposed volumetric rate shown in figure 5. We observe that the axial pressure gradient is very nearly periodic with a phase different from that of the volumetric flow rate. In fact, keeping in mind the discussion of §4.1, we infer that the flow lags the driving pressure gradient by approximately 90°. This is in agreement with the findings of Uchida (1956). Figure 6(*b–f*) shows the flow-field development. Referring to the secondary flow, we observe a vortex appearing almost in the middle of the core immediately above the centre of the pipe. The magnitudes of the secondary velocities on the cross-section are such that the vortex is a very weak one. These features, i.e. the existence of the vortex, the location of its centre and its weak strength, prevail qualitatively throughout the cycle, as if the secondary flow were steady. That this is not the case for all aspects of the flow can be seen from figure 12(*a*), where the circumferential shear stress along the circumference of the pipe is plotted for a sequence of times through the cycle. The unsteady nature of the secondary streaming is evident. Upon deceleration, the axial velocity reverses direction shortly after $\omega t^* = \frac{1}{2}\pi$. That this is no coincidence can be deduced from the pressure gradient, figure 6(*a*). At $\omega t^* = \frac{1}{2}\pi$ the slope of the pressure gradient is almost zero and about to reverse direction, changing from an adverse to a favourable gradient. (Again, note that the actual pressure gradient which drives the flow is the negative of what is plotted in part (*a*) of figures 6–10.) The inertial forces are out of phase with the viscous forces. The interaction of the two is such that the net axial flow at this time starts reversing its direction. At $\omega t^* = \pi$ the backflow occupies a region of thickness about one third of the radius along the wall and extending as far as the outer wall. Upon acceleration, the fluid gains enough momentum to be swept downstream thus eliminating any reverse-flow region.

Overall, the secondary flow patterns observed over the cycle for $Re_m = 1$ resemble a Dean-type secondary flow as described by Dean (1927, 1928), Smith (1975, 1976) and Lin & Tarbell (1980). Instead of the frequency parameter α, Smith, and Lyne (1971) used a parameter β which is related to α by the equation $\beta = \sqrt{2}/\alpha$. From this we calculate that for $\alpha = 15$, $\beta = 0.0943$. From table 2 we see that the secondary Reynolds number for $Re_m = 1$ is $R_s = 6.349 \times 10^{-4}$. These conditions are closely approximated by Case III of Smith's (1975) study for $\beta \ll 1$, $\kappa_m = O(1)$ and $R_s \ll 1$. According to this case, as stated by Smith, the 'problem reverts to the conventional Dean problem'. Owing to the low value of the mean Dean number, $\kappa_m = 0.7559$, or mean Reynolds number, the flow exhibits the simplest of the Dean-type secondary flow characteristics as outlined by Smith: the Stokes layer along the wall and the interior core. Together they constitute a single vortex over the half-cross-section centrifuging fluid outward along the centreplane and recirculating it along the pipe wall.

Another feature to be noted is that throughout the cycle the maximum axial velocity is located slightly off the centre towards the inner bend. This was also observed by Bertelsen & Thorsen (1982) and Mullin & Greated (1980). However, no conclusion can be drawn from these facts as the conditions of those investigations were quite different from ours. For example, Bertelsen & Thorsen solved the problem of a sinusoidal flow with zero mean and, in addition, their frequency parameter was larger than ours. Mullin & Greated's work used parameter values closer to ours but with frequency parameter still significantly lower.

Extending the mean Reynolds number to larger values, we obtain the results of figure 7(*a–f*) for $Re_m = 200$. The vortex whose centre earlier had been located right above the centre of the pipe moves closer to the wall. Encountering the boundary

layer which forms along the wall, the vortex is forced to mushroom out spreading toward both the inner and the outer bend. This motion of the vortex dominates the secondary flow and enhances the gradients in the boundary layer reducing it further in thickness. When the accelerative phase begins, all of the secondary flow patterns are significantly reduced in magnitude.

Referring to the axial isovelocity contours it is interesting to notice that although, like for $Re_m = 1$, the largest region of backflow occurs at $\omega t^* = \pi$, it now shows a tendency to collect in the inner portion of the pipe. The region of backflow, which extended along the wall all the way from the inner to the outer bend and was about one-third of the radius thick for $Re_m = 1$, has now decreased significantly in thickness from $\phi = \frac{1}{2}\pi$ to the outer bend ($\phi = 0$). To compensate for this decrease in thickness practically the whole inner half of the pipe is filled with fluid of negative axial velocity.

The mushrooming of the vortex is even more dramatic and its effect on the rest of the flow very pronounced for $Re_m = 300$ (figure 8*a–f*). We observe that from as early into the cycle as $\omega t = \frac{1}{4}\pi$ (figure 8*b*), the flow has a tendency to rotate near the centre in a fashion counter to the way it has before, i.e. the fluid tends to move inward, at least in part of the neighbourhood of the centre. The centre appears as a sink for part of the fluid around it. This portion of the fluid escapes from the small region right above the centre. This motion near the centre can be attributed to a suction effect caused by the faster moving fluid further away from the centre. From the isovelocity contours we infer that a good deal of the core is largely inviscid. From the secondary-velocity vectors we see that the fluid moves faster further away from the centre and immediately ahead of the 'centre' of the vortex. A direct application of Bernoulli's equation tells us that the pressure is higher at the centre than it is below the vortex. This pressure imbalance gives rise to a suction effect. The fluid immediately below the vortex moves outward. The vectors through the third grid points show that the outward-going fluid moves almost tangentially along the circumferential direction. These vectors form a streamline which approaches the centreplane almost at right angles. Owing to the symmetry of the flow there is a similar streamline coming from the lower half of the cross-section. When these two streamlines meet, they give rise to a flow similar to a stagnation-point flow pattern. The flow splits into two parts, one moving toward the outer bend and one toward the centre. The pressure gradient pushing the fluid inward is large enough in this region near the centre to overcome the outward-directed centrifugal force pushing the fluid outward. It is this force imbalance that is responsible for the inward-moving fluid in this part of the neighbourhood of the centre. As the deceleration period continues, the vortex concentrates closer to the inner bend (see, e.g. $\omega t^* = \frac{3}{4}\pi$). In so doing it gives rise to a shear layer in the vicinity of the centre and toward the inner-bend side, as shown in figure 8(*d*), for $\omega t^* = \pi$. This shear layer persists throughout most of the acceleration period. Throughout this period any existing secondary flow becomes significantly weaker, but still persists. On the other hand, we observe a dramatic change evolving from $\omega t^* = \frac{3}{2}\pi$ to $\omega t^* = \frac{7}{4}\pi$. The very small vortex which started appearing where the centreplane intersects the inner bend at $\omega t^* = \frac{3}{2}\pi$ spreads out to a much larger size at the next time, $\omega t^* = \frac{7}{4}\pi$. Thus far most of the faster-moving fluid along the axial direction has been located closer to the outer bend. From figure 8(*f*), for $\omega t^* = \frac{7}{4}\pi$, it is evident that the axial velocity has increased dramatically compared with its values at the previous time; in fact, it has almost doubled. This increase in the axial velocity, along with its spreading out to cover

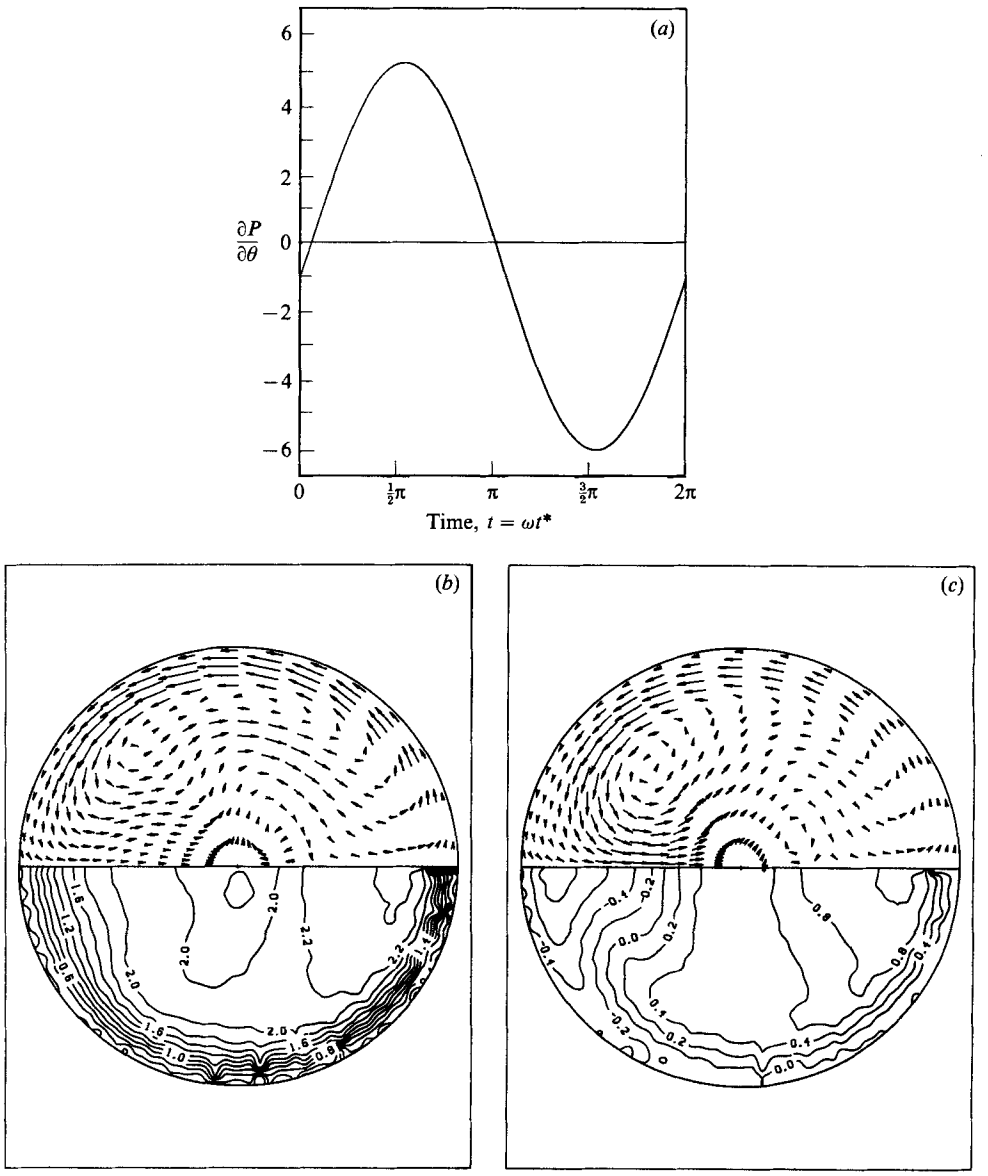

FIGURE 8(*a–c*). For caption see facing page.

almost the entire cross-section, weakens completely any existing secondary flow pattern. Finally, we note from figure 8(*e*) that the boundary layer caused by the secondary streaming separates in the neighbourhood of the inner bend and gives rise to a small vortex in that region. This is the first sign of boundary-layer separation in the secondary flow.

Clearly, the results for $Re_m = 300$ mark a transition to much more complex flow patterns. Looking at the flow-field development for $Re_m = 400$, figure 9(*a–f*), we see that the mushrooming effect of the vortex originally at 90° has become more pronounced. It results in a vortex at the inner bend, and one located toward the outer bend early on into the cycle (figure 9*b*). What we described for the previous Reynolds number as a stagnation-point flow on the centreplane located toward the

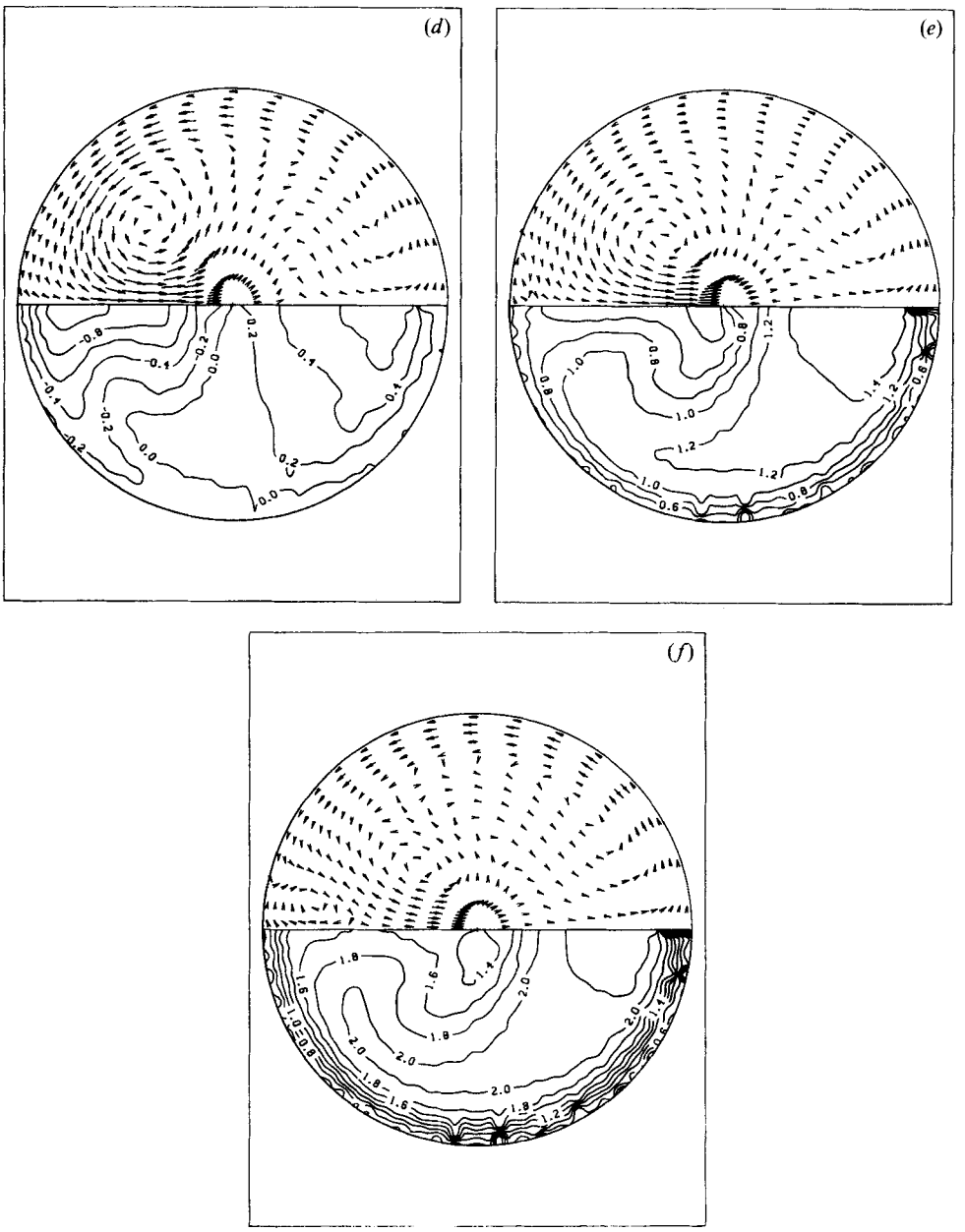

FIGURE 8. (*a*) Calculated axial pressure gradient for $Re_m = 300$. (*b–f*) Secondary-velocity vectors and axial isovelocity contours for $Re_m = 300$, $\lambda = 0.4$: (*b*) $\omega t^* = \frac{1}{4}\pi$; (*c*) $\frac{3}{4}\pi$; (*d*) π; (*e*) $\frac{3}{2}\pi$; (*f*) $\frac{7}{4}\pi$.

outer bend, has now moved further outward resulting in an inward flow at the right-half of the vicinity of the centre. We note that $Re_m = 300$ marks a transition, in the half-cross-section, from a two-vortex to a three-vortex flow pattern. Up to $Re_m = 300$ we have two main vortices characterizing the flow: one that rotates the fluid from the inner bend to the outer bend along the centreplane, which then returns along the wall forming a boundary layer, and one that is located at about $\phi = \frac{1}{2}\pi$. The latter is located near the centre at low Reynolds numbers. As the Reynolds number

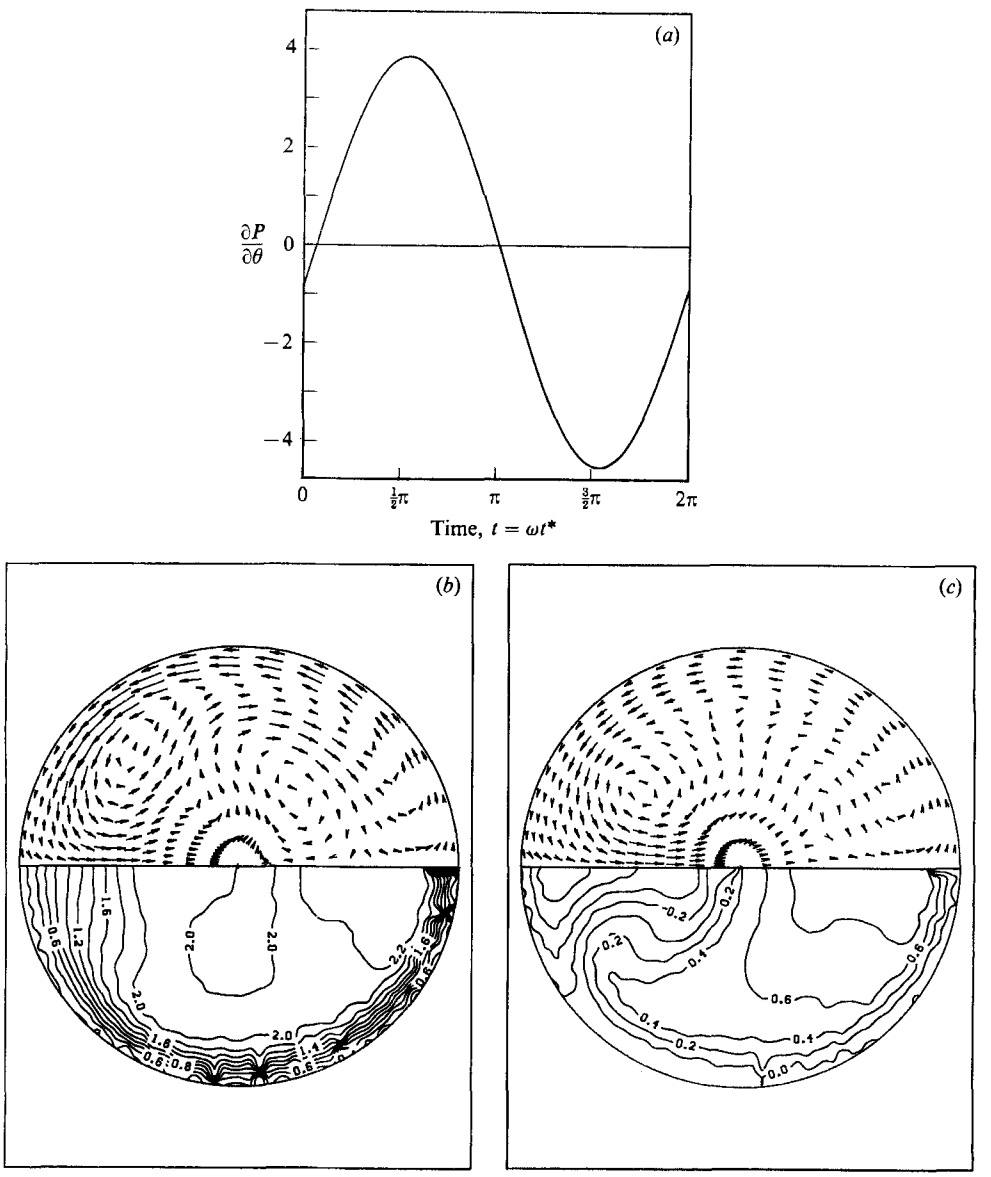

FIGURE 9(a–c). For caption see facing page.

increases it moves towards the wall almost along the $\phi = \frac{1}{2}\pi$ line. At about $Re_m = 300$ the motion of this vortex encounters a pressure gradient in the boundary layer too large to overcome. It is forced to mushroom out toward both the inner and outer bends giving rise to two vortices, located in the vicinity of each bend. Of the two vortices the one located near the inner bend seems to be the dominant one, since whereas this one persists for most of the cycle, the other has completely disappeared by $\omega t^* = \frac{3}{4}\pi$. At $\omega t^* = \frac{3}{2}\pi$ the secondary flow has lost its strength almost completely and the secondary boundary layer separates at the inner bend. This phenomenon was first observed at $Re_m = 300$, occurring at the same time as here, $\omega t^* = \frac{3}{2}\pi$. The boundary-layer separation results in a vortex being generated at the inner bend. This vortex expands outward to almost half the radius at $\omega t^* = \frac{7}{4}\pi$. At this time we can

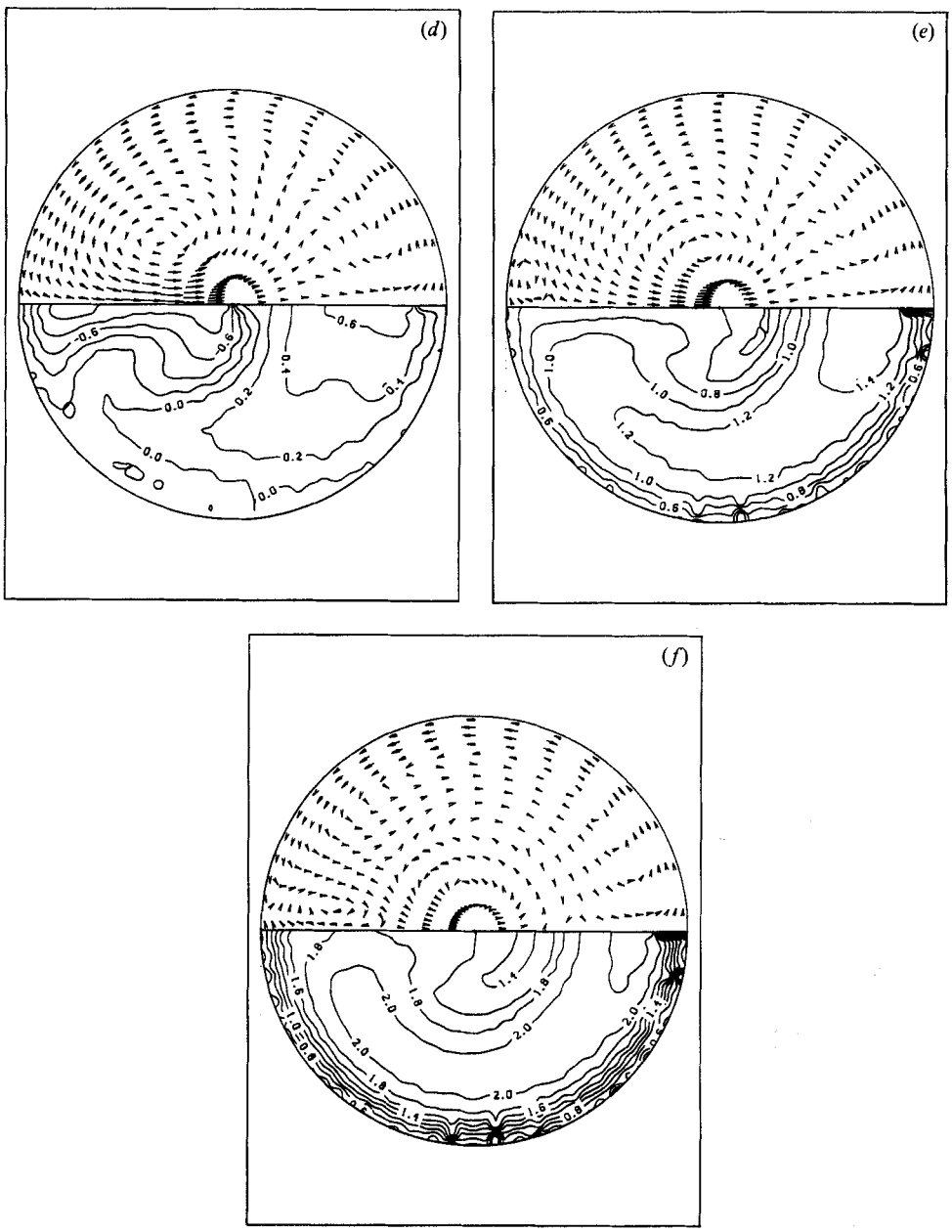

FIGURE 9. (*a*) Calculated axial pressure gradient for $Re_m = 400$. (*b–f*) Secondary-velocity vectors and axial isovelocity contours for $Re_m = 400$, $\lambda = 0.3$: (*b*) $\omega t^* = \frac{1}{4}\pi$; (*c*) $\frac{3}{4}\pi$; (*d*) π; (*e*) $\frac{3}{2}\pi$; (*f*) $\frac{7}{4}\pi$.

also see clearly what Gong terms a 'ridge', a region of fast moving fluid bounded on both sides by slower moving fluid. This can be seen from the isovelocity contours, and the extent of the contour labelled 2.

At $Re_m = 1000$, figure 10(*a–f*), we observe a rather interesting phenomenon. The strong vortex that appears at about $\phi = 130°$ at $\omega t^* = \frac{1}{4}\pi$ and that has not thus far appeared to be totally independent of the rest of the flow, begins to exhibit the tendency to become so. Notice how it is only a very narrow region on the upper side

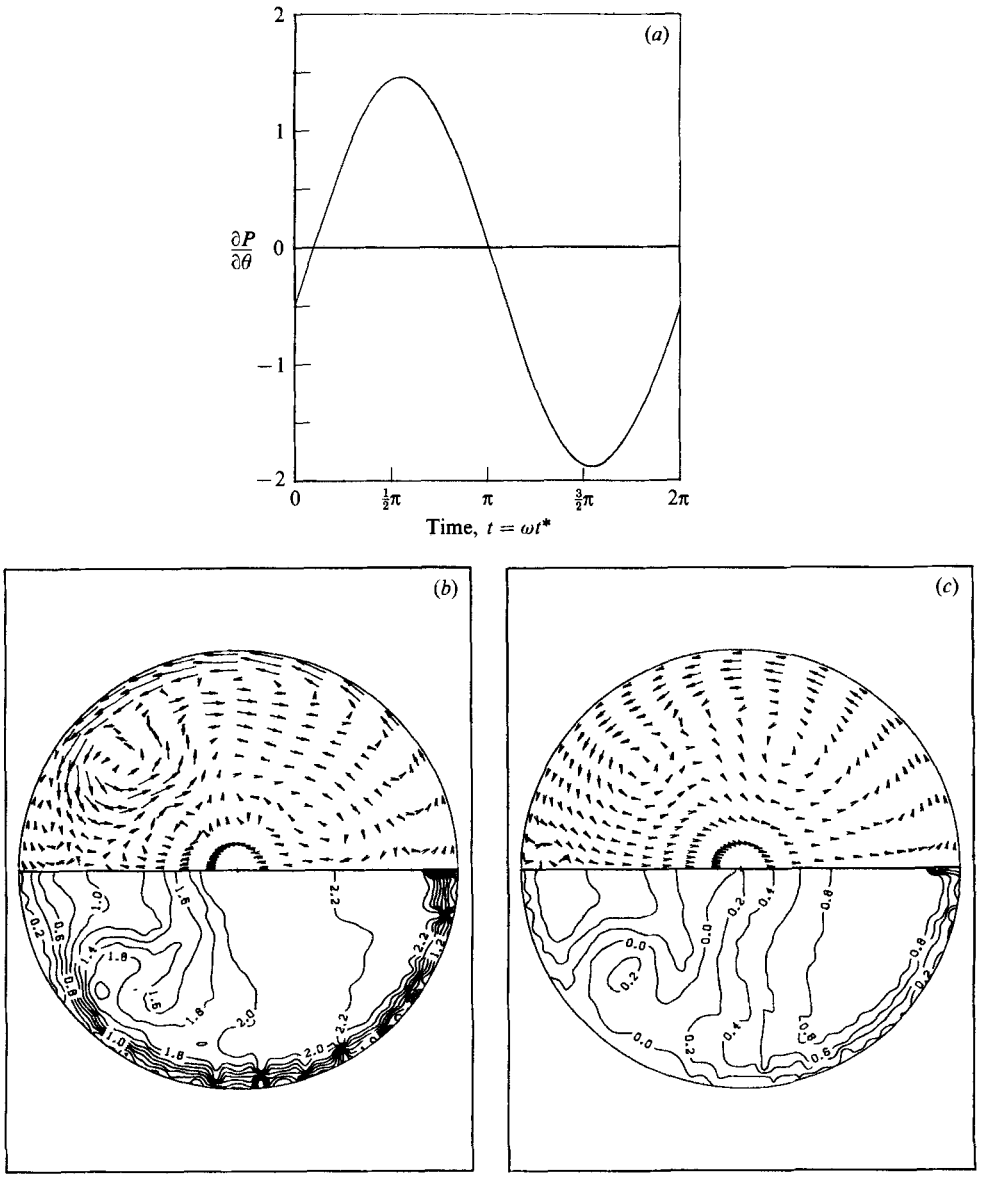

FIGURE 10(*a–c*). For caption see facing page.

of this vortex in which the fluid gets entrained, and escapes from the vortex. Because of the axial velocity any existing vortex in three dimensions implies a helical motion. If the axial velocity were absent, a vortex would consist of the same portion of fluid circulating around the centre of the vortex. This vortex, however, to which we have been referring (usually called the *Dean vortex*) is not closed, and the fluid within it is continuously renewed by fluid from outside the vortex. For the first time we observe a tendency of this vortex to be closed, and so were it not for the axial velocity the same lump of fluid would continue circulating around. Indeed, this vortex does become closed at $\omega t^* = \frac{1}{2}\pi$. In reference to the points made at the end of the discussions for $Re_m = 300$ and 400 regarding the separation of the secondary boundary layer at the inner bend at about $\omega t^* = \frac{3}{2}\pi$, we note that for $Re_m = 1000$ the

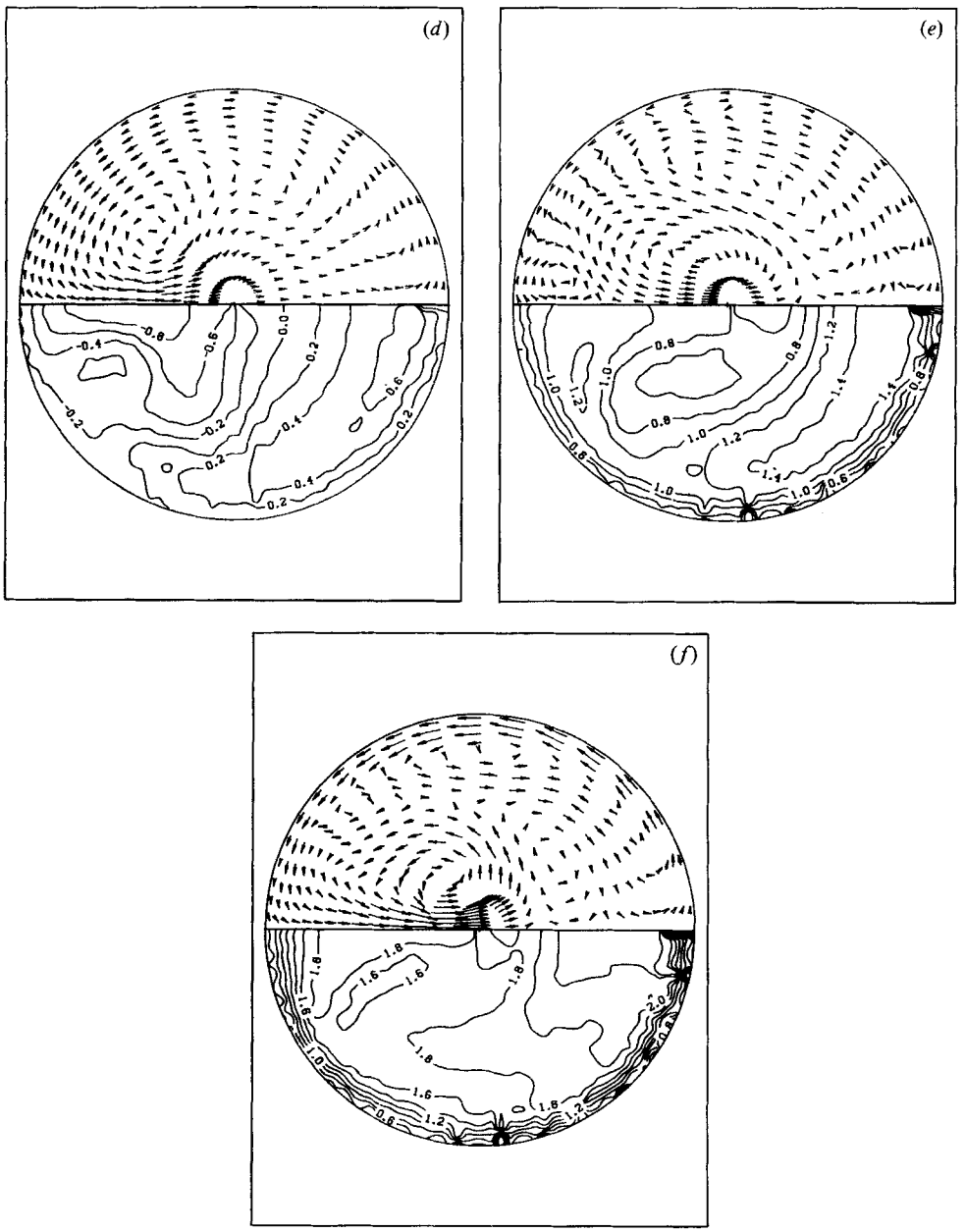

FIGURE 10. (*a*) Calculated axial pressure gradient for $Re_m = 1000$. (*b–f*) Secondary-velocity vectors and axial isovelocity contours for $Re_m = 1000$, $\lambda = 0.4$: (*b*) $\omega t^* = \frac{1}{4}\pi$; (*c*) $\frac{3}{4}\pi$; (*d*) π; (*e*) $\frac{3}{2}\pi$; (*f*) $\frac{7}{4}\pi$.

separation occurs again in the neighbourhood of the inner bend. There are, however, the following two differences: (*a*) the separation occurs now from the very beginning of the cycle and is seen in figure 10(*b*) for $\omega t^* = \frac{1}{4}\pi$; (*b*) the point of separation has moved farther away from the inner bend than where it was for $Re_m = 300$ and 400.

Up to $Re_m = 300$ the fluid experiences an outward centrifuging-type of secondary motion similar to that observed by Dean (1927, 1928) for a steady pressure gradient

along the pipe. For $Re_m = 300$, or $\kappa_m = 226.8$, for the first time we observe a tendency for the flow in the interior to behave in the opposite sense to that predicted for the steady case. This type of behaviour was first reported by Lyne (1971) in the limit $\alpha \to \infty$. Lyne observed this kind of unexpected secondary motion in this limit of α for both small and large values of Reynolds number. It should, however, be kept in mind that Lyne's work is valid for a pipe whose radius of curvature is assumed large compared with its cross-sectional radius, and for axial pressure gradients which are sinusoidal in time with zero mean. In this same paper Lyne also presented experimental data in support of his theoretical results. In his experiment the parameters had the values $\delta = 0.075$, $\epsilon = 0.18$, $R_s \approx 24$, $\beta = 0.05$. We have used $\delta = \frac{1}{7} = 0.1429$, $\epsilon = 1.0942$, $R_s = 25.4$, $\beta = 0.0943$. Note that our δ is twice that of Lyne. These values have been obtained for the case $Re_m = 200$, for which, from table 2, we have that $R_s = 25.4$. The parameters β and ϵ relate to ours by the following expressions: $\beta = \sqrt{2}/\alpha$, $\epsilon = \beta(\frac{1}{2}R_s)^{\frac{1}{2}}$. Our results for $Re_m = 200$, figure 7(a–f), however, do not indicate any inward secondary flow. This is attributable to the differences in the values of the determining parameters.

Bertelsen (1975) carried out an experimental investigation with $\delta = 0.1$. He concluded that Lyne's work was valid for $R_s \leqslant 2$ provided that $\alpha \geqslant 10$. Munson (1975) performed experiments for $\delta = 0.637/8.89 = 0.0717$, imposing an oscillating axial pressure gradient. He presented results for the range $0.7 < \alpha < 32$. We note first that Munson also used a value of δ lower than ours and an oscillating pressure gradient with, presumably, zero mean. He correlated his secondary Reynolds number R_s to α and δ by $R_s = 1.0609\alpha^2\delta$. The last two figures he presented are for $\alpha = 10.7$ and $\alpha = 21$. These correspond to $R_s = 8.7127$ and $R_s = 33.56$, respectively, using the above expression and the value of δ that he used. It is for the last set of these data that he got agreement with Lyne and observed a reversal of the secondary flow, from the outside towards the inside of the bend at the pipe centre. This can be compared to our flow patterns for $Re_m = 300$. The small discrepancy in the values of the parameters at which this happens arises from the difference in curvature ratios, and by the fact that Munson used a pressure gradient with zero mean, which we did not.

The work of Smith (1975) is of particular significance as the only theoretical work on oscillating curved-pipe flows with a non-zero mean pressure gradient. He imposed a pulsating pressure gradient of the form

$$\frac{\partial p}{\partial(R\theta)} = -[\rho\omega\overline{W}\cos(\omega t^*) + G],$$

where all variables are in their dimensional form, and $\overline{W}$ is a characteristic velocity. The parameters he uses are β (discussed earlier), R_s, defined in the manner we have (see table 1), and $D = Ga^3\delta^{\frac{1}{2}}/\rho\nu^2$, related to our parameters by

$$D = 2\frac{G}{\rho\omega\overline{W}}\frac{\omega a^2}{\nu}\kappa_m = 2\frac{G}{\rho\omega\overline{W}}\alpha^2\kappa_m.$$

He also states the relationship $R_s = \frac{1}{2}(2\kappa_m)^2\beta^2$ between κ_m, R_s, and β. The ratio $G/\rho\omega\overline{W}$ is the ratio of the magnitude of the steady (or direct) component of the pressure gradient to that of the unsteady (or alternating) part. From part (a) of figures 6–10, we find that this ratio has the values 0.0889, 0.0889, 0.1000, 0.1064 and 0.1500 for the values $Re_m = 1$, 200, 300, 400, and 1000, respectively. The corresponding values of the parameter D are 10.0013, 2000, 3375, 4788, and 16875. The value of β is

$\sqrt{2}/\alpha = 0.0943$, for $\alpha = 15$. From the above relation for R_s, we find the corresponding values $R_s = 0.0011$, 44.4625, 100.0405, 177.8498 and 1111.6. The conditions of $Re_m \geqslant 200$ are best approximated by case IX of Smith's analysis, one of his two analyses where the direct and the alternating components of the axial pressure gradient are of comparable magnitude. Case IX requires that $\beta = nD^{-\frac{1}{6}}$ and $R_s = \frac{1}{2}\lambda^2 n^2 D$. For $Re_m = 200$, 300, 400, 1000 we get that $n = 0.3347$, 0.3652, 0.3871, 0.4776, respectively. Smith comments that 'this has been the first example of a core/boundary-layer motion in which the secondary streaming is also largely unsteady, an occurrence connected with the actions of the pressure gradient, whose steady and unsteady parts are here of comparable magnitude'. Indeed, such signs of unsteadiness have been observed in our results for $Re_m \geqslant 200$. Also, Smith points out that for n 'small the pulsatility becomes $\frac{1}{2}\pi$ out of phase with the pressure gradient and the secondary streaming may exhibit reversals in direction during each time cycle, owing to the enhanced effect of the frequency of oscillation'. These features have been observed in our results too and have been discussed earlier.

4.3. *Shear-stress development*

We now look at the results for the two components of shear stress for each mean Reynolds, or mean Dean, number separately, and how they evolve in time. In figures 11 (*a–d*) and 12 (*a–d*) the left-hand side, $\phi = 0$, corresponds to the outer bend and the right-hand side, $\phi = \pi$, to the inner bend.

4.3.1. *Evolution of axial shear stress with Dean number as a function of time*

Figure 11 (*a*) shows that for $\kappa_m = 0.7559$, or $Re_m = 1$, regions of negative axial flow appear only in the time interval $\frac{1}{2}\pi < \omega t^* < \pi$. When they occur they span the entire region adjacent to the wall extending from the inner to the outer bend. The maximum axial shear stress is observed at $\omega t^* = 5.4978 = \frac{7}{4}\pi$ at the inner bend in a positive flow region. The axial shear stress maintains the same patterns up to about $\kappa_m = 75.59$, or $Re_m = 100$.

Figure 11 (*b, c*) shows that the axial shear stress for higher Reynolds numbers exhibits the same behaviour. The main difference is that we now observe separation in the axial velocity, first occurring very near the outer bend and spreading inward as the Reynolds number is increased. In addition, the maximum value of the stress is nearly uniformly distributed throughout the entire circumferential direction along the wall, moving from the inner bend, where it was located for $Re_m = 1$, outwards. It has moved nearly to the outer bend at $\kappa_m = 756.0$ (figure 11*d*) and now occurs at an even later time than previously, at the end of the cycle, $\omega t^* = 2\pi$.

Rabadi *et al.* (1980) reported similar results. They imposed a pressure gradient of the form $\partial p/\partial\theta = 1 + k\cos(\omega t^*)$ for $k = 1$. For $1 \leqslant \alpha \leqslant 15$, $\delta = 0.01$ and $Re = 100$ their results show that the maximum local axial wall shear stress occurs at the outer bend. Rabadi *et al.* do not show any negative values for their axial velocity, but the problem they studied is different from ours, as can be seen from the values of parameters listed above, and comparison cannot be made with our results. Figure 11 (*a–d*) shows quite clearly that for those periods of time within the cycle for which no backflow occurs, the maximum local axial shear stress is located at the inner bend only for $Re_m = 1$, or $\kappa_m = 0.7559$ (figure 11*a*). In contrast, it is located at the outer bend for the remainder of the values of Reynolds number studied (figure 11*b–d*). Considering now the periods of time within the cycle that reversal of the axial velocity is observed (backflow), we see from figure 11 (*a–d*) that the maximum absolute local values of the axial shear stress are invariably located at the

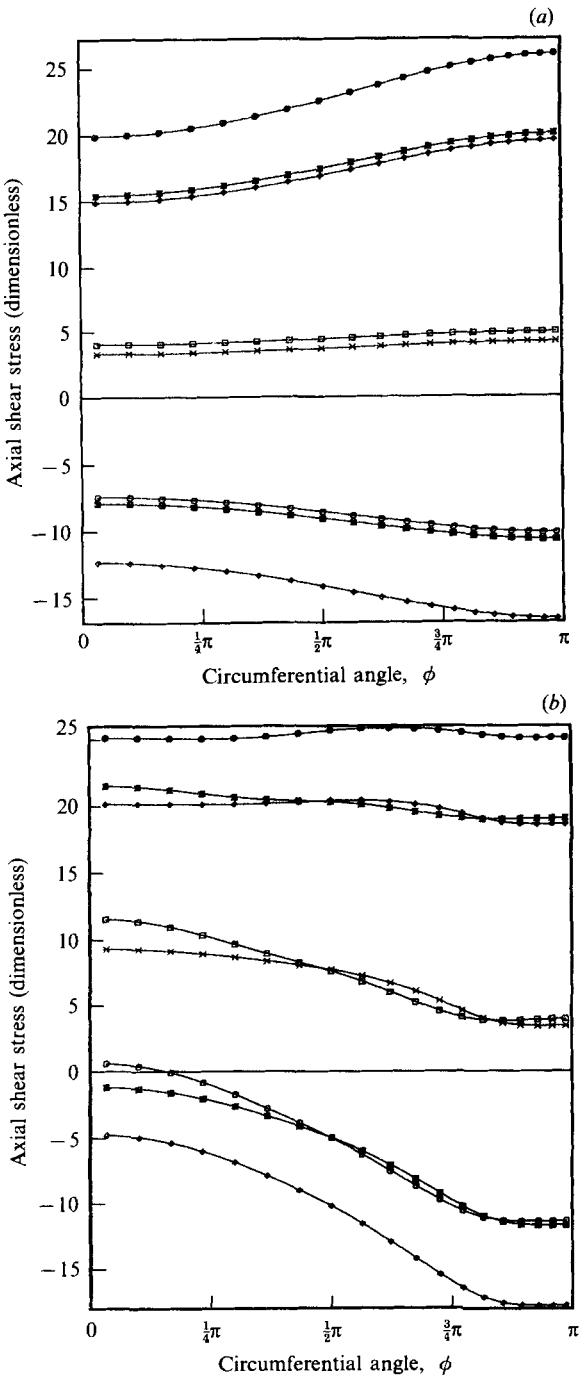

FIGURE 11(*a*,*b*). For caption see facing page.

inner bend. In fact, these values are quite sizeable compared with the maximum value that is observed in any of these figures. Thus the region of backflow is quite intense, the high velocities being evident in those parts of figures 6–10 that show reverse axial flow.

Similar results were obtained also by Singh, Sinha & Aggarwal (1978) theoretically, and by Choi *et al.* (1979) experimentally. Both of these works, however, deal with the

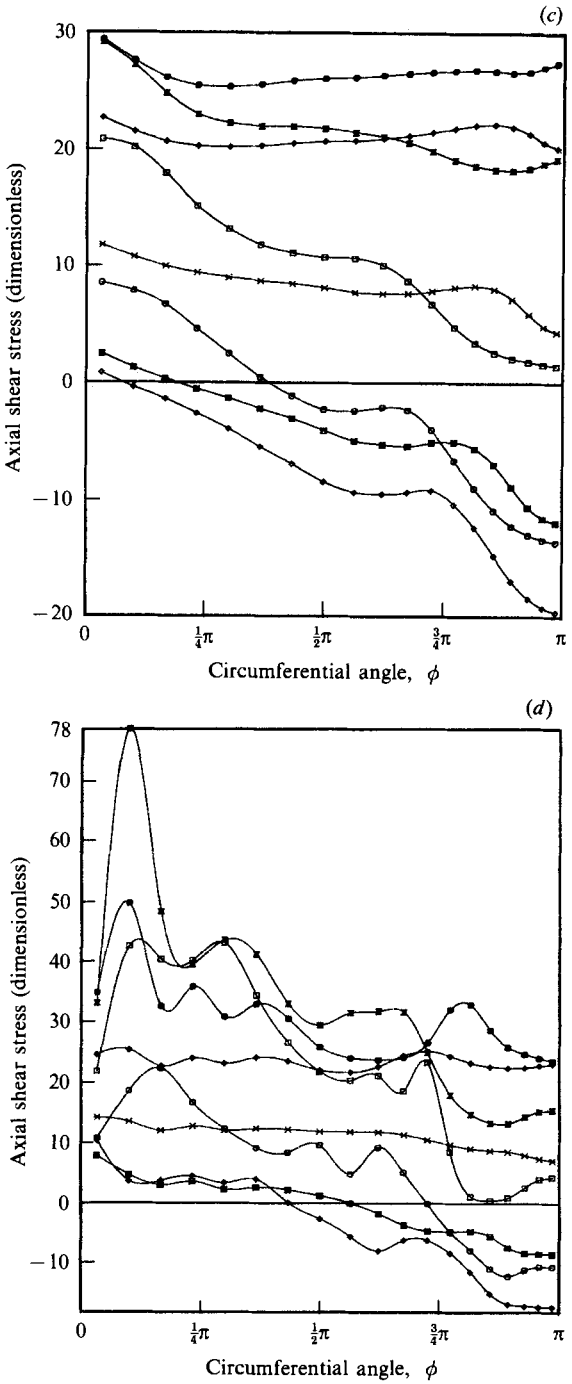

FIGURE 11. Axial shear stress for (*a*) $Re_m = 1$, $\kappa_m = 0.7559$; (*b*) $Re_m = 200$, $\kappa_m = 151.2$; (*c*) $Re_m = 400$, $\kappa_m = 302.4$; (*d*) $Re_m = 1000$, $\kappa_m = 756$. Times plotted: □, $\frac{1}{4}\pi$; ○, $\frac{1}{2}\pi$; ◇, $\frac{3}{4}\pi$; ⊠, π; ×, $\frac{5}{4}\pi$; ⊕, $\frac{3}{2}\pi$; ⊕, $\frac{7}{4}\pi$; ⧖, 2π.

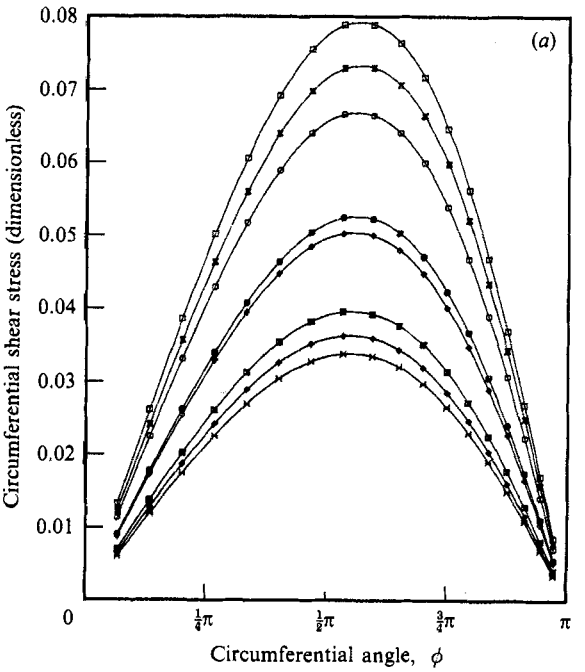

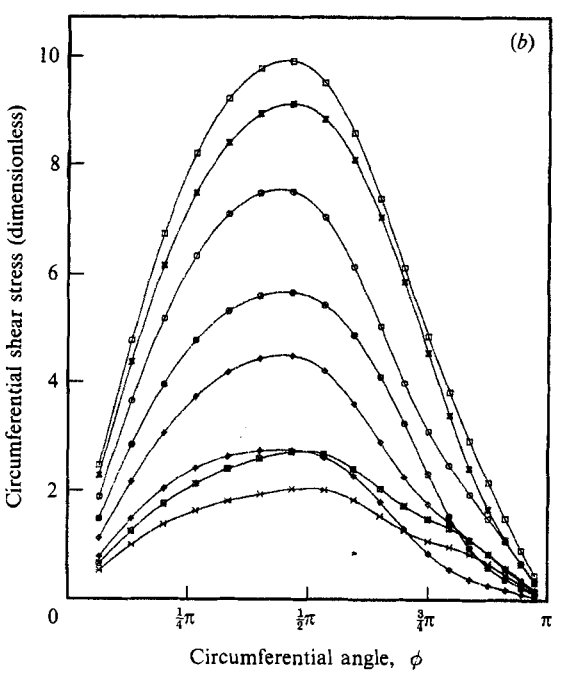

FIGURE 12(*a*,*b*). For caption see facing page.

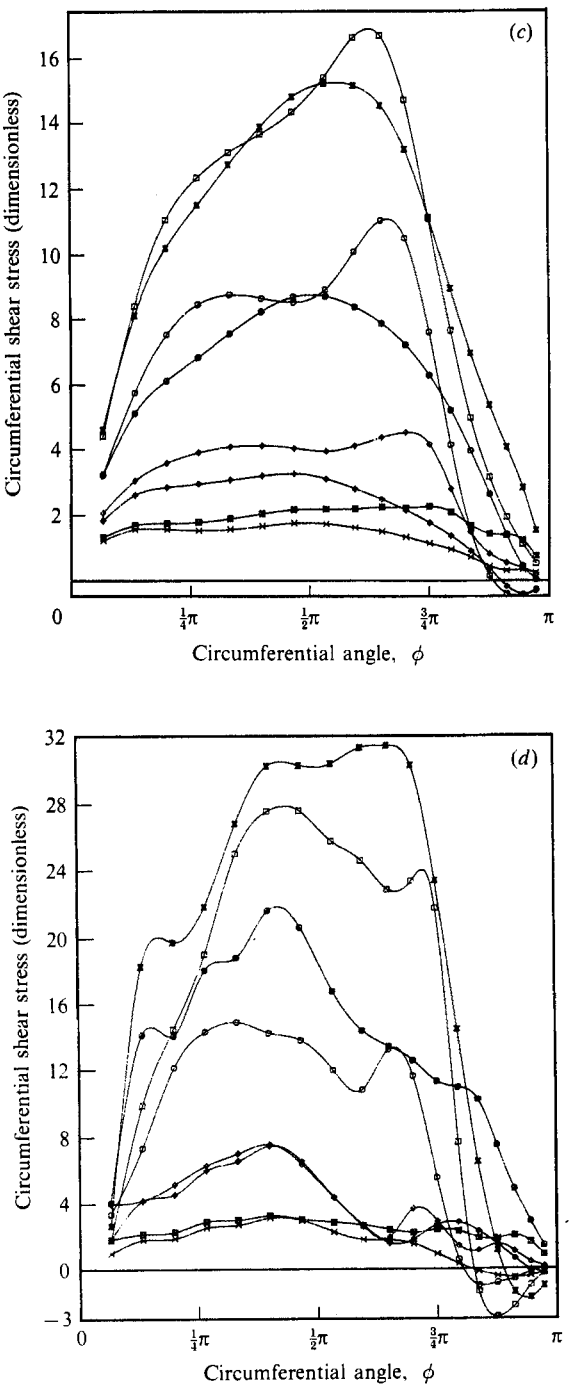

FIGURE 12. Circumferential shear stress for (*a*) $Re_m = 1$. $\kappa_m = 0.7559$; (*b*) $Re_m = 200$. $\kappa_m = 151.2$; (*c*) $Re_m = 400$. $\kappa_m = 302.4$; (*d*) $Re_m = 1000$. $\kappa_m = 756$. For the legend see figure 11 caption.

entry region of a curved pipe. Whereas the latter study considered steady flows only, the former treated periodic flows with a volumetric flow rate similar to ours and is closer to our work.

4.3.2. *Evolution of circumferential shear stress with Dean number as a function of time*

Figure 12(*a*, *b*) covering the range $0.7559 < \kappa_m < 151.1860$, or $1 < Re_m < 200$, shows that the maximum value of circumferential shear stress at all times during the cycle occurs at $\phi \approx \frac{1}{2}\pi$, considerably toward the inner bend for $Re_m = 1$, and considerably toward the outer bend for $Re_m = 200$. Separation of the secondary flow is observed in figure 12(*c*, *d*). Once again, we see how complicated the flow becomes upon interaction of the vortex, initially near the centre at low Reynolds numbers, with the boundary layer at the wall. The resulting mushrooming of the vortex during the transition regime of Reynolds numbers is made evident by the extent in the circumferential direction in which high values of shear stress occur. Whereas in figure 12(*a*, *b*) the maximum value manifests itself in a narrow and rather sharp peak, and located slightly off-centre towards the outer bend, this is not the case in figure 12(*c*, *d*) and maximum shear stress occurs over most of the region along the wall. The number of local maxima and minima present in figure 12(*c*, *d*) suggests the presence of a vortex structure with several pairs of vortices.

Figure 12(*a*, *b*) shows that up to $Re_m = 200$, or $\kappa_m = 151.1860$, the secondary flow is well behaved and consists of one vortex, and that the maximum value of the circumferential shear stress shifts from the inner bend (near $\phi = \frac{1}{2}\pi$) to the outer bend (near $\phi = \frac{1}{2}\pi$) as the Reynolds number is increased. This is due to the shift of the centre of circulation of the secondary flow. Rabadi *et al.* (1980) found a considerable shift in the location of the local maximum value of the circumferential shear stress toward the inner bend as the secondary flow became more intense, i.e. as the frequency parameter α was increased. In our case the secondary flow becomes more intense with Reynolds number and the shift in the location of the maximum circumferential shear stress is opposite to that reported by Rabadi *et al.* This is attributed to the fact that they used $\delta = 0.01$, and $Re = 100$. Rabadi *et al.* also point out that local wall-shear-stress variations with time depend strongly on α and k. (For the definition of k see §4.3.1.)

Comparing the values of the two components of shear stress, we see that although the contribution of the circumferential component is negligible compared with that of the axial one for $Re_m = 1$, for $Re_m \geqslant 200$, or $\kappa_m \geqslant 151.1860$, the contribution of the circumferential component is almost as large as 50% of that of the axial one. This is due solely to the strengthening of the secondary flow with Reynolds number. Yet further evidence regarding the strong effect of the secondary flow is provided by the peaks and valleys in the wall-shear profile. Such peaks and valleys are clearly evident in figures 11(*c*), 11(*d*), 12(*c*) and 12(*d*), i.e. for $Re_m \geqslant 400$, or $\kappa_m \geqslant 302.4$, and are indicative of the strong effect of the secondary flow. Their appearance for this range of Reynolds numbers is consistent with the expectation (see §2.1) that the strength of the secondary flow increases with Reynolds number.

5. Conclusion

The fully developed region of sinusoidal flows through curved pipes of arbitrary curvature has been investigated. The effect of Reynolds number on the flow has been analysed for the range $1 \leqslant Re_m \leqslant 1000$. The values of the frequency parameter,

$\alpha = 15$, curvature ratio, $\delta = \frac{1}{7}$, and amplitude ratio, $\gamma = 1$, have been chosen to simulate blood flow through the aortic arch (Gong 1979) and have been kept constant throughout the calculations. Our results agree very well qualitatively with previous theoretical, numerical and experimental investigations. They reveal a series of interesting phenomena concerning both the secondary and axial flows. The principal results can be summarized as follows:

(i) The secondary flow exhibits a Dean-type motion with one vortex in each half-cross-section, located near the centre at low values of Reynolds numbers; for larger Reynolds numbers the vortex moves towards the wall, where, encountering the boundary layer, it is forced to mushroom out giving rise to a much more complex secondary flow.

(ii) The reversal of the secondary flow from outward, 'centrifuging' or Dean-type motion, to inward, or Lyne-type motion, occurs at about $Re_m = 300$.

(iii) At low Reynolds number the maximum axial velocity is located off-centre toward the inner bend. This location shifts outwards as the Reynolds number increases.

(iv) The axial flow is reversed in a portion of the cross-section for $\frac{1}{2}\pi \leqslant \omega t^* \leqslant \frac{5}{4}\pi$. The region of negative axial flow becomes maximum for $\omega t^* = \pi$. It occupies an area of width approximately one third of the radius and spans the entire region along the wall, extending from the inner to the outer bend for $Re_m = 1$. As the Reynolds number increases it moves toward the inner wall and eventually occupies the entire inner half of the cross-section at $\omega t^* = \pi$.

(v) Regarding the axial shear stress, for the periods of time during which the axial flow is unidirectional and positive, its maximum is located at the inner bend for $Re_m = 1$, whereas for larger Reynolds number it shifts to the outer bend. During periods that the axial flow ceases to be unidirectional the area of local maximum shear stress is invariably located at the inner bend, indicating strong local reversal of the flow.

(vi) In regard to the circumferential shear stress for $Re_m = 1$ and 200, its local maximum for all times throughout the cycle is located at $\phi \approx \frac{1}{2}\pi$, slightly towards the inner bend for the former and slightly toward the outer bend for the latter. For $Re_m > 200$ more than one local maxima and minima are observed; an indication of the existence of a vortex structure with several pairs of vortices.

Searching for an understanding of the flow of blood in the aortic arch and the physiological conditions leading to atherosclerosis has for a long time been a major driving factor behind advances in our knowledge of the patterns and properties of flows through curved pipes. The present work may be relevant in explaining phenomena such as cholesterol build-up in the aortic walls. For example, it is the inner bend of the aorta that is most severely affected by the disease (Texon 1980). For high-Reynolds-number flows, pertinent to conditions in the aorta, our results show that backflow occurs and occupies the inner half of the cross-section at $\omega t^* = \pi$. At the inner section, when the axial flow is unidirectional, i.e. only positive axial flow, the axial shear stress is a minimum; when backflow is present, it is a maximum. The net effect over the cycle may be a deposition of cholesterol. This matter needs to be studied further to complement the work of Chang & Tarbell (1985) who did similar work imposing a physiological pressure gradient.

In closing, we mention another point of concern, namely that of symmetry. It was not until recently that Winters (1984) and Winters & Brindley (1984) reported that the condition of symmetry should be viewed with caution, at least for fully developed steady flows, for they find asymmetric solutions arising from a symmetry-breaking

bifurcation point. They also find that all multiple solutions, except the two-cell ones, are unstable with respect to either symmetric or asymmetric perturbations. No such finding has been reported, yet, for unsteady flows. This raises the issue of multiple solutions irrespective of symmetry. Yang & Keller (1986), Nandakumar & Masliyah (1982) and Dennis & Ng (1982) have all reported the existence of multiple solutions for steady flows. These studies all imposed the symmetry condition and yet all reported multiple solutions. While this evidence, for steady flow, is not directly relevant to our unsteady analysis, it does call for further work to see if a similar situation arises for unsteady flows.

The authors wish to acknowledge the support and assistance of Professors Lawrence Talbot and Alexander Chorin of the University of California at Berkeley. They are also particularly grateful for the help and advice of Dr W. Y. Soh of NASA Lewis Research Center.

This material is based upon work supported by the National Science Foundation under Grant No. MEA-8116360 and ECE-8417852.

REFERENCES

AGRAWAL, Y. C. 1975 Laser velocimeter study of entrance flows in curved pipes. Ph.D. thesis, University of California, Berkeley.

AGRAWAL, Y. C., TALBOT, L. & GONG, K. 1978 Laser anemometer study of flow development in curved circular pipes. *J. Fluid Mech.* **85**, 497.

ALLEN, J. S. & CHENG, S. I. 1970 Numerical solutions of the compressible Navier–Stokes equations for the laminar near wake. *Phys. Fluids* **13**, 37.

BERGER, S. A., TALBOT, L. & YAO, L.-S. 1983 Flow in curved pipes. *Ann. Rev. Fluid Mech.* **15**, 461.

BERTELSEN, A. F. 1975 An experimental investigation of low Reynolds number secondary streaming effects associated with an oscillating viscous flow in a curved pipe. *J. Fluid Mech.* **70**, 519.

BERTELSEN, A. F. & THORSEN, L. K. 1982 An experimental investigation of oscillatory flow in pipe bends. *J. Fluid Mech.* **118**, 269.

CARO, C. G., FITZ-GERALD, J. M. & SCHROTER, R. C. 1971 Atheroma and arterial wall shear. Observation, correlation and proposal of a shear dependent mass transfer mechanism for atherogenesis. *Proc. R. Soc. Lond.* B **177**, 109.

CHANG, L.-J. & TARBELL, J. M. 1985 Numerical simulation of fully developed sinusoidal and pulsatile (physiological) flow in curved tubes. *J. Fluid Mech.* **161**, 175.

CHOI, U. S., TALBOT, L. & CORNET, I. 1979 Experimental study of wall shear rates in the entry region of a curved tube. *J. Fluid Mech.* **93**, 465.

CHORIN, A. J. 1968 Numerical solution of the Navier–Stokes equations. *Maths Comp.* **22**, 745.

DEAN, W. R. 1927 Note on the motion of fluid in a curved pipe. *Phil. Mag.* **4**, 208.

DEAN, W. R. 1928 The stream-line motion of fluid in a curved pipe. *Phil. Mag.* **5**, 673.

DENNIS, S. C. R. & NG, M. C. 1982 Dual solution for steady laminar flow through a curved tube. *Q. J. Mech. Appl. Maths* **35**, 305.

DOUGLAS, J. 1962 Alternating direction methods for three space variables. *Numer. Maths* **4**, 41.

DOUGLAS, J. & GUNN, J. E. 1964 A general formulation of alternating direction methods. Part I. Parabolic and hyperbolic problems. *Numer. Maths* **6**, 428.

FRY, D. L. 1968 Acute vascular endothelial changes associated with increased blood velocity gradients. *Circulat. Res.* **22**, 165.

FRY, D. L. 1973 Responses of the arterial wall to certain physical factors. In *Atherogenesis: Initiating Factors. Ciba Symposium*, vol. 12, p. 93. North-Holland: Elsevier, Excerpta Medica.

GONG, K. O. 1979 Experimental study of unsteady entrance flow in a curved pipe. Ph.D. thesis, University of California, Berkeley.

HAMAKIOTES, C. C. 1987 Fully developed pulsatile flow in a curved tube. M.Sc. thesis. University of California, Berkeley.

ITŌ, H. 1987 Flow in curved pipes. *JSME Intl J.* **30**, 543.

LIN, J. Y. & TARBELL, J. M. 1980 An experimental and numerical study of periodic flow in a curved tube. *J. Fluid Mech.* **100**, 623.

LYNE, W. H. 1971 Unsteady viscous flow in a curved pipe. *J. Fluid Mech.* **45**, 13.

MULLIN, T. & GREATED, C. A. 1980 Oscillatory flow in curved pipes. Part 2. The fully developed case. *J. Fluid Mech.* **98**, 397.

MUNSON, B. R. 1975 Experimental results for oscillating flow in a curved pipe. *Phys. Fluids* **18**, 1607.

NANDAKUMAR, K. & MASLIYAH, J. H. 1982 Bifurcation in steady laminar flow through curved tubes. *J. Fluid Mech.* **119**, 475.

NANDAKUMAR, K. & MASLIYAH, J. H. 1986 Swirling flow and heat transfer in coiled and twisted pipes. In *Advances in Transport Processes*, vol. 4 (ed. A. S. Mujumdar & R. A. Masliyah). Wiley Eastern.

NEREM, R. 1981 Arterial fluid dynamics and interactions with the vessel walls. In *Structure and Function of the Circulation*, vol. 2 (ed. C. J. Schwartz, N. T. Werthessen & S. Wolf). Plenum.

RABADI, N. J., SIMON, H. A. & CHOW, J. C. F. 1980 Numerical solution for fully developed, laminar pulsating flow in curved tubes. *Numer. Heat Transfer* **3**, 225.

SCHETTLER, G., *et al.* Eds. 1983 *Fluid Dynamics as a Localizing Factor for Atherosclerosis.* Springer.

SINGH, M. P. 1974 Entry flow in a curved pipe. *J. Fluid Mech.* **65**, 517.

SINGH, M. P., SINHA, P. C. & AGGARWAL, M. 1978 Flow in the entrance of the aorta. *J. Fluid Mech.* **87**, 97.

SMITH, F. T. 1975 Pulsatile flow in curved pipes. *J. Fluid Mech.* **71**, 15.

SMITH, F. T. 1976 Fluid flow into a curved pipe. *Proc. R. Soc. Lond.* A **351**, 71.

SOH, W. Y. 1983 Laminar entrance flow in a curved pipe. Ph.D. thesis, University of California, Berkeley.

TALBOT, L. & GONG, K. O. 1983 Pulsatile entry flow in a curved pipe. *J. Fluid Mech.* **127**, 1.

TEXON, M. 1980 *Hemodynamic Basis of Atherosclerosis.* Hemisphere.

UCHIDA, S. 1956 The pulsating flow superposed on the steady laminar motion of incompressible fluid in a circular pipe. *Z. angew. Math. Phys.* **7**, 403.

WINTERS, K. H. 1984 A bifurcation study of laminar flow in a curved tube of rectangular cross-section. *Harwell Rep.* AERE-TP. 1104.

WINTERS, K. H. & BRINDLEY, R. C. G. 1984 Multiple solutions for laminar flow in helically-coiled tubes. *Harwell Rep.* AERE-R. 11373.

YANG, Z. & KELLER, H. B. 1986 Multiple laminar flows through curved pipes. *Appl. Numer. Maths* **2**, 257.

ZALOSH, R. G. & NELSON, N. G. 1973 Pulsating flow in a curved tube. *J. Fluid Mech.* **59**, 693.